Design and fabrication of hybrid carbon nanotube - $NbSe_2$ devices for Majorana Fermion detection

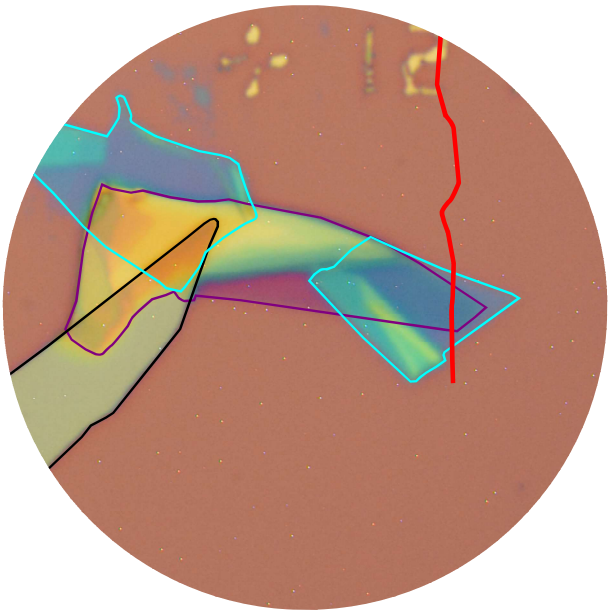

THESIS

submitted in partial fulfillment of the
requirements for the degree of

MASTER OF SCIENCE
in
PHYSICS

Author :	Brecht G. Simon
Student ID :	s1392778
Supervisor :	Prof. Dr. Ir. Tjerk H. Oosterkamp
External supervisors :	Dr. Nicola Paradiso
	Prof. Dr. Christoph Strunk

Leiden, The Netherlands, August 24, 2018

Design and fabrication of hybrid carbon nanotube - $NbSe_2$ devices for Majorana Fermion detection

Brecht G. Simon

Huygens-Kamerlingh Onnes Laboratory, Leiden University
P.O. Box 9500, 2300 RA Leiden, The Netherlands

August 24, 2018

Abstract

Majorana quasiparticles can arise at the ends of one dimensional superconducting quantum wires. As a true one-dimensional experimental realization of such a quantum wire, a carbon nanotube can be employed. The one-dimensional carbon nanotube can inherit the superconducting properties by bringing it in close contact to a superconductor, such as van der Waals superconductor niobium diselenide. In this work, the design and fabrication of devices are discussed that contain a carbon nanotube connected to a few atomic layer thick niobium diselenide. Bi- or trilayers of niobium diselenide crystal flakes are obtained using mechanical exfoliation techniques in inert conditions. A stamping resolution of about 1 μm is obtained in positioning the flakes with respect to each other which is shown by Atomic Force Microscopy. Initial characterizations have shown an improvement of the conductance of more than two orders of magnitude. The stability diagrams, however, exhibit a complex behaviour which we were unable to explain in terms of a proximitized carbon nanotube. We have shown that it is possible to fabricate the complete hybrid device that is predicted to host Majorana Fermions in its non-trivial phase.

This work was conducted at Regensburg University in the group of Professor Christoph Strunk.

Contents

Chapter 1

Introduction

In 2016, Thouless, Kosterlitz and Haldane were awarded with the Nobel Prize for physics for their work on topological phase transitions and topological states of matter. These physicists are considered pioneers of an emergent field in physics reffered to as topology in condensed matter. The most famous manifestations of these new states of matter are the integer and the fractional Quantum Hall effect [1].

Analogue to the well known Landau theory, topology describes phase transitions between many body quantum states. Landau theory describes phase transitions in systems that exhibit spontaneous symmetry breaking, with magnetism and superconductivity as famous examples. From Landau theory, we are used to describe these phase transitions in terms of an order parameter. In topology, however, transitions between topological states of matter, between trivial and non-trivial phases, cannot be described by an order parameter. The concept of topological invariant is used instead [2].

In topology, two systems are equivalent when they can be continuously deformed into each other [1]. Applied to Hamiltonian physics, it means that two systems are topologically equivalent when the parameters of the system can be tuned continuously without changing the system's relevant symmetries, i.e. without closing the bulk energy gap [2]. In case of a non-zero topological invariant, the system is said to be topologically non-trivial. This invariant is calculated for the bulk system by taking into account all filled bands. At the edges of such a non-trivial system, at the boundaries to a trivial state, zero energy, gapless states must form. These resulting edge states are protected against small perturbations of the bulk. The properties of the edge states are determined by the bulk, often referred to as the bulk-edge correspondence.

1.1 Majorana Fermions

The study of topology and its invariants have been found extremely useful in the search for systems that can host Majorana quasi-particles. In superconducting systems, such quasiparticles appear, under special conditions, as combinations of electron and hole excitations [3]. Such

Majorana Fermions (MFs) obey the relation [4]:

$$\gamma = \gamma^{\dagger} \tag{1.1}$$

where γ and $\gamma^{\dagger}$ are the annihilation and creation operators. Particles obeying this relation have already been predicted in 1937 [4]. Because of the Majorana property, MFs are fermions which are their own anti-particles. Every fermionic operator can be written in terms of a pair of Majorana modes γ_1, γ_2, [2]:

$$c^{\dagger} = \frac{1}{2}(\gamma_1 + i\gamma_2) \tag{1.2}$$

$$c = \frac{1}{2}(\gamma_1 - i\gamma_2) \tag{1.3}$$

where $c^{\dagger}$ and c describe the creation or the annihilation of an electron. Since in condensed matter systems, the particle degree of freedom is determined by the number of electrons, only pairs of MFs exist. We also know that when particles combine with their anti-particles, they annihilate. In order to prevent annihilation of all MFs into ordinary electrons, MFs must be separated in space. One way to establish a pair of non-degenerate MFs separated in space is the one-dimensional superconducting quantum wire, proposed by Kitaev [5].

1.2 Majorana Fermions in semiconducting nanowires

In his seminal paper, Kitaev showed that a one-dimensional chain of spinless superconducting fermionic modes can host MFs [2, 5]. At the Fermi energy ($E = 0$), the superconductor that introduces the particle anti-particle symmetry: $\gamma(E) = \gamma^{\dagger}(-E)$, ensures the Majorana property from equation 1.1[3]. The proposed superconducting pairing mechanism, however, relies on a p-wave character, rather then on the conventional s-wave superconductivity found in most materials. This is a consequence of the spinless model. The p-wave pairing mechanism is proportional to momenta resulting in an inter-pair coupling in real space. A consequence of inter-pair coupling is illustrated in Fig. 1.1. If the inter-pair coupling is strong enough, single Majorana end modes appear, separated from each other by the bulk.

Figure 1.1: Chain of fermionic modes and corresponding Majorana pairs for different coupling regimes Blue ellipses represent the trivial phase, where the pair coupling is strong. Red ellipses represent the non-trivial phase, where the inter-pair coupling exceeds the pair coupling.

Instead of waiting for material scientists to provide with such an exotic superconductor, proposals were formulated where an effective p-wave pairing emerges as an effect of spin-orbit interaction. This strong spin-orbit coupling is able to lift the spin degeneracy while still enabling Andreev reflections at the interface to induce a proximity effect. With the theoretical designs and computations of these hybrid devices, experimentalists are now able to fabricate such systems and realize the Majorana zero end modes [6, 7].

1.2.1 Experimental realization systems hosting Majorana Fermions

Hallmarks of MFs, have only recently been observed experimentally in proximitized semiconducting nanowires [6]. In this design, a small magnetic field perpendicular to the spin-orbit field and parallel to the wire axis, lifts the degeneracy of the states at $k = 0$, as can be seen in Fig. 1.2a. For a certain range of the magnetic field and the chemical potential a non-trivial state is expected: two Majorana modes at the edges of the nanowire (*). In Fig. 1.2b, the experimental realization of this design is illustrated: The green gate is used to create a tunnelling barrier at the border between the normal wire and the proximitized part of the wire. The bias voltage is defined between the normal lead (N) (gold), the normal wire (indium antiminode) and the proximitized part of the wire to the superconducting lead (S) (niobium titanium nitride). Gates 1-4 are used to change the chemical potential in different parts of the superconducting wire.

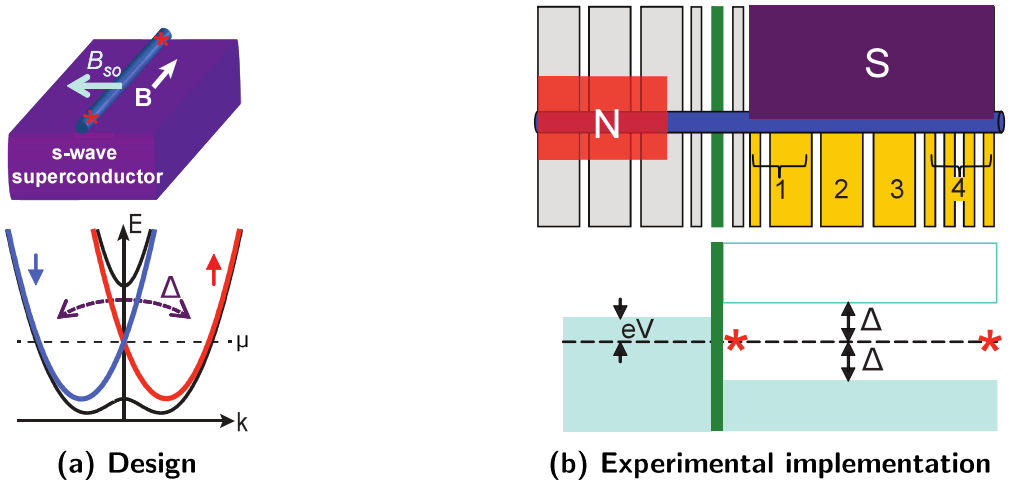

(a) Design (b) Experimental implementation

Figure 1.2: Design by Mourik et al. for MFs in semiconducting nanowires Figure (a) shows an effective p-wave superconducting quantum wire that can be realized by a semiconducting nanowire with strong spin-orbit interaction that is proximitized by a conventional s-wave superconductor. In the non-trivial phase Majorana modes appear at the ends of the wire. Figure (b) shows the experimental implementation of the conceptual device in order to measure the conductance as a function of gate voltage. Conductance of the indium antimonide nanowire is measured (blue wire). The nanowire is connected by one normal (gold) contact (red) and one superconducting niobium titanium nitride electode (purple). The green gate before the edge of the normal to superconducting wire is used to define a tunnel junction for spectroscopy measurements. Only the left Majorana mode is probed in this set-up [6].

Figure 1.3, shows the differential conductance measurement for different magnetic field strengths. In this tunneling spectroscopy set-up, the differential conductance is a measure of the density of states inside the superconducting wire. At zero magnetic field, peaks at -200 and $200\,\mu$V represent the gap of the superconductor. Between 100 mT and 400 mT a zero bias peak appears inside the superconducting gap. The long range for which the peak remains at zero bias shows that the modes are stable against perturbations of the magnetic field. The results from Mourik *et al.* show the possibility to reach a non-trivial topological state in a semiconducting nanowire and to measure the signatures of the resulting zero energy modes in a spectroscopy measurement.

1.3 Thesis outline

Due to the great promises of employing the non-Abelian exchange properties of Majorana fermions for future topological quantum information processing, much research is conducted on the realization of MFs in different systems [1, 8].

The devices designed and fabricated in this thesis are based on the theoretical proposal by Marganska *et al.* [8]. In their proposal, a new system is introduced that is predicted to host Majorana quasi particles. This system consists of a semiconducting carbon nanotube (CNT) proximitized by an ultra thin superconductor. In their design, few layer niobium diselenide ($NbSe_2$) introduces the superconductivity. Van der Waals material $NbSe_2$ can be exfoliated down to a single atomic layer. The usage of an ultra thin superconductor allows one to electro statically tune its chemical potential. Similar to the nanowire in the experimental design of Mourik *et al.*, the CNT exhibits spin-orbit coupling. The corresponding pseudo magnetic field is aligned parallel to the tube's axis. For some special conditions, such as the presence of a magnetic field, the proximitized tube is predicted to have a non-trivial phase. In this non-trivial phase Majorana modes are expected to appear at the ends of the wire. In this work, mechanical exfoliation techniques in inert conditions are used to open the $NbSe_2$ crystal flake down to a bi- or trilayer and to transfer the flake on top of a substrate containing a CNT. A few layer dielectric material is added in order to produce the high electric fields necessary to tune the chemical potential inside the superconductor. Different devices have been fabricated and characterized by atomic force microscopy. Finally, the first preliminary transport measurements, conducted by PhD candidate Christian Bäuml, are reported in the result section.

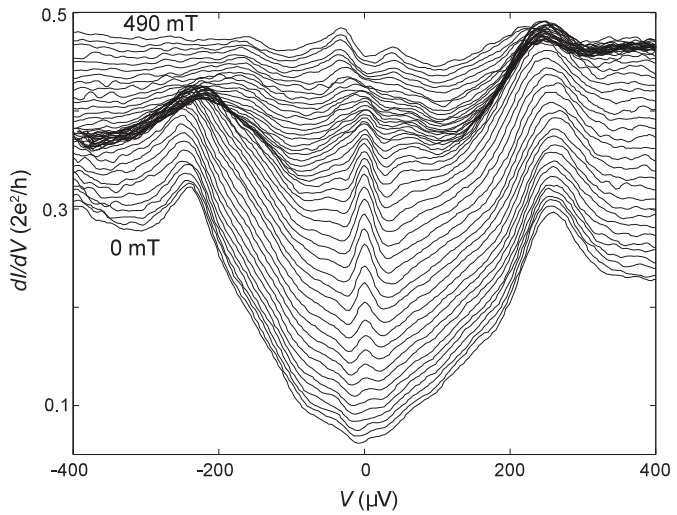

Figure 1.3: Differential conductance measurements as a function of bias voltage for different magnetic field strenghts, as measured by Mourik et al. [6] Due to the tunnel junction, the conductance measurements in this set-up are a measure of the density of states in the proximitized wire. For a certain magnetic field range, subgap features start appearing. A single gap feature at zero energy points at the presence of a MF at the edge of the wire.

Chapter 2

Theory

This chapter describes the realization of MFs in semiconducting CNTs based on the theoretical proposal by Marganska *et al.*, 2018 [8]. Its individual components are a one-dimensional CNT that is proximitized by a gate tuned $NbSe_2$ flake. We will briefly discuss in the first section the individual components: the CNT, proximity-induced superconductivity and the layered material $NbSe_2$. Following this section, we describe the combination of the different components to obtain a hybrid device whose non-trivial phase is predicted to host MFs.

2.1 Individual components of the hybrid device

2.1.1 Carbon nanotubes

The structure of a cylindrical carbon nanotube can be described in terms of a rolled up graphene sheet, as can be seen from fig. 2.2. Therefore, most of the properties known from graphene, that is well studied, can be translated to carbon nanotubes. Graphene consists of sp^2-hybridized carbon atoms, resulting in a two-dimensional hexagonal lattice. A stack of graphene sheets, bounded together by the van der Waals force gives rise to common graphite. A single atomic layer of graphite, called graphene, can therefore be obtained by simply cleaving the crystal mechanically [9]. The atomic and reciprocal lattice structure of graphene and its corresponding dispersion is shown in Fig. 2.1.

Tight-binding calculations of the graphene lattice give rise to accurate models of the electronic dispersion which is shown in Fig. 2.1c. For zero doping, the Fermi surface is made out of the six points at the corners of the Brillouin zone where the valence and conduction bands touch [10].

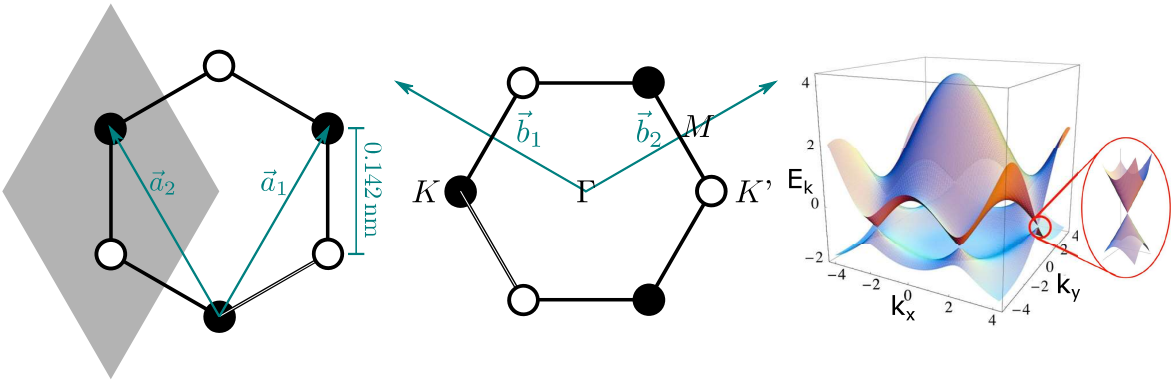

(a) Atomic structure **(b) Reciprocal structure** **(c) Electronic dispersion graphene**

Figure 2.1: Graphene structure and electronic properties In Fig. (a) atomic lattice and the lattice basis vectors, $\vec{a}_1$ and $\vec{a}_2$ of graphene are illustrated. The lattice constant is given by: $a = \sqrt{3}a_{c-c} = 246\,\text{nm}$. The shaded grey area represents de unit cell of the graphene carbon lattice. In Fig. (b), the reciprocal graphene lattice vectors, $\vec{b}_1$ and $\vec{b}_2$, are illustrated. The K and K' points are due to rotational symmetry equal for graphene [11]. In Fig. (c), the three-dimensional electronic dispersion of graphene is plotted, showing the six K and K' points of high conductivity. Figure (c) is adopted from Castro Neto *et al.*, 2009 [12]

The electronic properties of the CNTs can then be deduced by an approximation that 'rolls' up the two-dimensional graphene lattice. How a graphene sheet is ideally rolled up to a tube determines the diameter and the chirality of the tube. The chiral vector, $\vec{C}$, is the vector along which the CNT is rolled up and around which the resulting circumference runs. In terms of the basis vectors of graphene it can be written as:

$$\vec{C} = n\vec{a}_1 + m\vec{a}_2 \tag{2.1}$$

where n and m are called the chiral indices[10]. The resulting diameter of the CNT can then be described as:

$$d = \frac{|C|}{\pi} = \frac{a}{\pi}\left(m^2 + mn + n^2\right)^{1/2} \tag{2.2}$$

with corresponding chiral angle:

$$\Theta = \arctan\left(\frac{\sqrt{3}m}{m+2n}\right) \tag{2.3}$$

Finally, the translational vector $\vec{T}$, which is defined in fig. 2.2a and $\vec{C}$ span the unit cell of the CNT [11].

The rolling imposes additional boundary conditions on the electronic wavefunctions. Depending on the chirality and the diameter, a single walled CNT can therefore have a different electronic dispersion. Therefore, different CNTs can be found to be either semiconducting or metallic. In practice, however, even nominally metallic CNTs show at least a tiny gap owing to additional perturbations [11]. The only CNTs perfectly metallic are the armchair ones of which the chiral indices are equal, $n = m$.

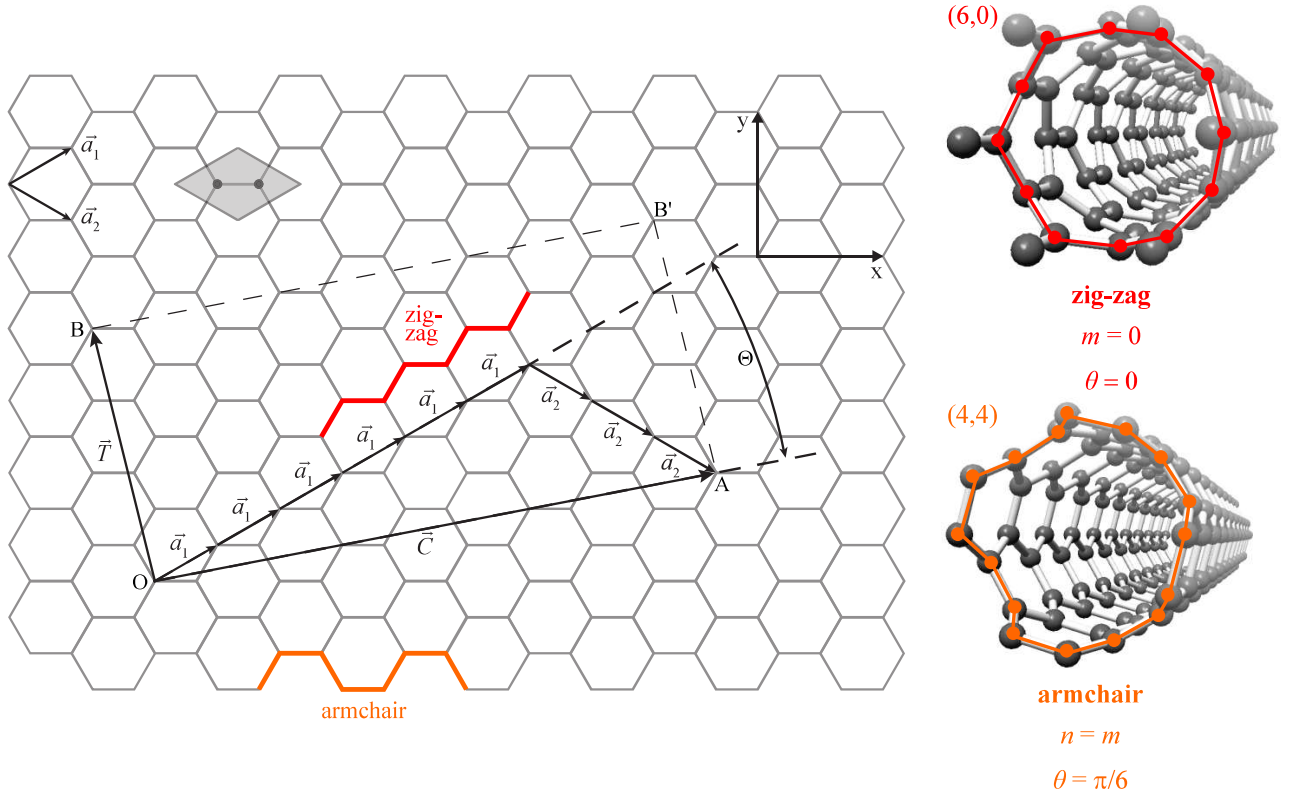

(a) Hexagonal graphene lattice **(b) Special types of CNTs**

Figure 2.2: Atomic structure CNT Figure (a) shows the hexagonal graphene lattice, where each corner point describes a carbon atom. The $\vec{T}$ and $\vec{C}$ vectors describe the different ways of rolling up the graphene as they span up the unit cell of the CNT. The $\vec{T}$ vector points along the axis of the tube, and $\vec{C}$ runs around the circumference. Chiral angle Θ is shown as well. Figure (b) is adopted from Gaass *et al.*, 2011 [10]. Figure (b) shows two special types of CNTs that are rolled up according to chiral indices $m = 0$ and $n = m$, resulting in the zig-zag and armchair CNTs respectively. Figure is adopted from Götz *et al.*, 2017 [11]

As the diameter of CNTs is generally small, electronic transport is one dimensional. Therefore, it is drastically affected by quantum effects and disorder. This results in a resistivity that is no longer constant with sample dimensions [10]. Different regimes of transport are often considered regarding carbon nanotubes: classical, (weakly/strongly) localized and ballistic transport. Ballistic transport is observed in high structural quality carbon nanotubes. In these tubes, the length over which the CNT is measured is much smaller than the mean free path and the phase coherence length of the electronic wave function. The conductance of such a tube is given by:

$$G = 2G_0 = \frac{4e^2}{h} = (6.4\text{k}\Omega)^{-1} \tag{2.4}$$

When the mean free path, L_M, is reduced as a result of diffusion, the electronic wave function is said to be localized. When also the phase correlation length is much smaller than the tube length, classical transport is dominant, as scattering events add up as a function of length [10]. Transport measurements are thus able to give a measure of how clean the nanotube is.

Moreover, although graphene does not exhibit spin-orbit interaction, the curvature of the carbon nanotube induces an effective spin-orbit interaction. Depending on the diameter, this can

result in a strong spin interaction, of which the corresponding pseudo magnetic field is oriented along the tube's axis [8].

2.1.2 Proximity-induced superconductivity

A crucial component in the realization of the Kitaev chain is the superconducting pairing term. Although the carbon nanotube is semiconducting, it can inherit superconducting properties by placing it in close proximity to a superconductor. A superconductor can be described by a condensate of Cooper pairs. A Cooper pair is a pair of electrons that forms a bound state due to an attractive potential. In conventional superconductors, this pairing occurs between electrons of opposite spin and momenta $\left(\vec{k}\uparrow, -\vec{k}\downarrow\right)$. A single Cooper pair can be considered as a Bose particle. A system of Bose particles follows the Bose-Einstein statistics, of which, below a certain critical temperature, all particles have the same identical ground state. All particles in this condensate, therefore, have identical wavefunctions, hereby describing a superfluid [13].

When a normal metal/semiconductor (N) and a superconductor (S) are brought in close contact, Cooper pairs from S can penetrate into N. This mechanism, in which single electron states incident at the N/S interface are converted into Cooper pairs is called Andreev reflection [14] and is illustrated in Fig. 2.3. In close contact, the Fermi energies of the normal metal and the superconductor align. For incoming electrons with $E > \Delta$, quasiparticle states present the superconductor sustain transport by means of normal scattering events. For $E < \Delta$, however, no quasiparticle states are available in the superconductor and the superconductor can not accept the electron. But, the superconductor is able to sustain a Cooper pair at the Fermi energy. A Cooper pair is, therefore, formed in the superconductor with $\left(\vec{k}\uparrow, -\vec{k}\downarrow\right)$ and in order to conserve momentum the incident electron with momentum $+k$ is retroreflected as a hole with momentum $+k$ [15].

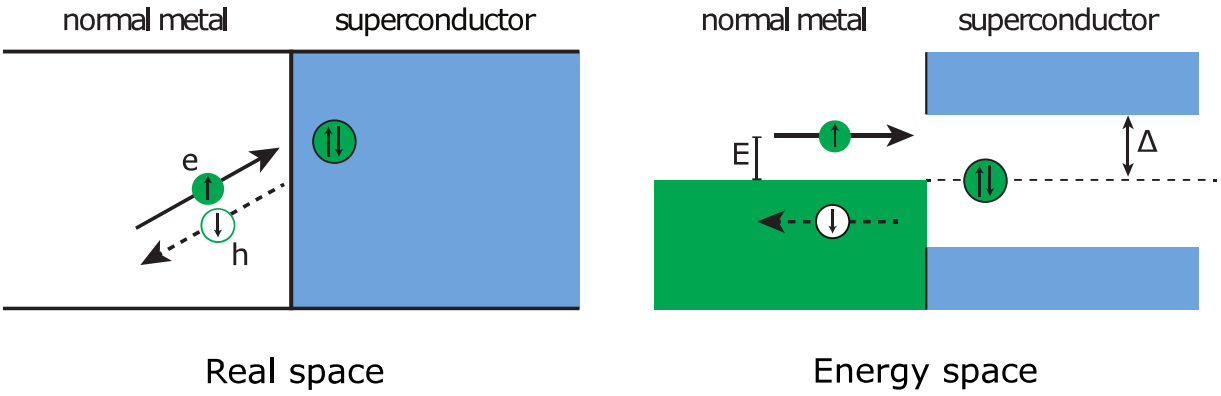

Figure 2.3: Schematic overview of Andreev reflection in real and energy space Transport below the gap occurs due to Andreev reflection of an electron that is retroreflected at the interface as a hole and a Cooper pair being formed in the superconductor at the Fermi energy. Figure adopted from Kjaergaard 2015 [15]

The mechanism of Andreev reflections described above assumes a perfect interface. In practice, such an interface is never completely transparent. A semiconductor, for example, has a much

lower carrier density than a superconductor resulting in a Fermi velocity mismatch at the interface [15]. Moreover, the fabrication process will almost always introduce some degradation of the interface. Such a non-ideal interface can be modelled as a tunnel junction between the NS interface, where a potential Z describes height of the tunnelling barrier [15].

In Fig. 2.4, the current and corresponding differential conductance across the NS interface is shown as a function of the bias for different values of Z. $Z = 0$ corresponds to a regime of perfect proximity-induced superconductivity and is represented by the red line plot. Inside the superconducting gap, an increase of twice the normal state conductance is a result of the Andreev process in which $2e$ is transferred across the interface. $Z > 0$ corresponds to a regime away from ideal promixity-induced superconductivity due to a tunneling barrier present at the interface. Inside the gap, transport no longer occurs due to Andreev reflections only, but also normal reflections of incident electrons occur, or electrons can be transmitted directly as quasi-holes or quasi-electrons [15]. Because the differential conductance measured in the tunneling regime ($Z > 0$) is proportional to the density of states of the system, the shape of the density of states of the superconductor is resolved and represented by the blue line plot [15].

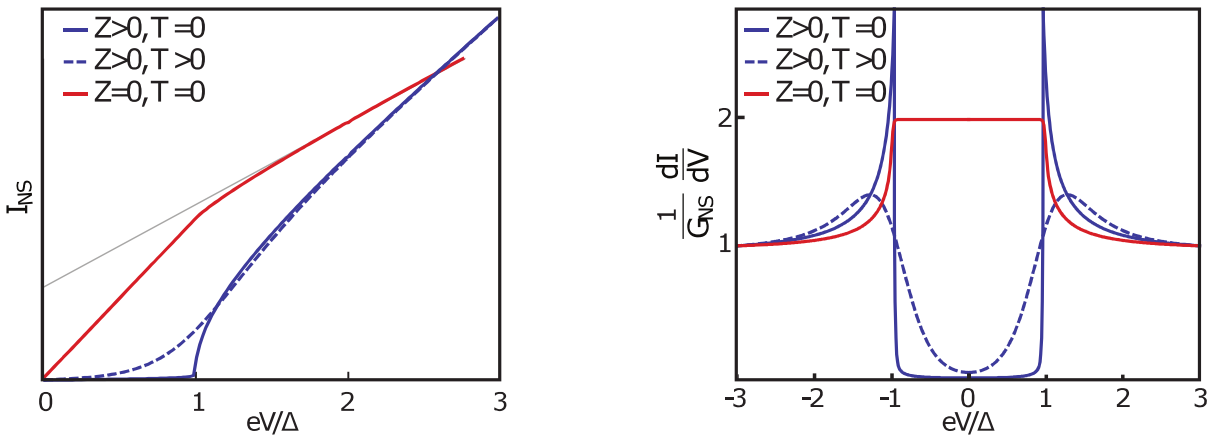

(a) Current **(b) Differential conductance**

Figure 2.4: Transport at a (non-)transparent NS interface Behaviour of the current and the corresponding differential conductance for different regimes of the transparancy (Z) of the junction in the superconducting state ($T = 0$) and above the superconducting temperature ($T > 0$). For $Z = 0$, the junction is transparent and for $Z > 0$ there is a potential barrier at the interface. For $Z > 0$ the differential conductance is a measure of the density of states. Figure adopted from Kjaergaard 2015 [15]

From fig. 2.4, it is clear that in the presence of a tunnel junction, the density of states of a system can be probed. In case of the presence of a MF in a (perfectly) promixitized CNT, a tunnel junction can be added at the end of wire in order to observe the density of states and the zero-energy subgap feature associated with the presence of a MF in a conductance measurement.

2.1.3 Niobium diselenide

In the proposal of Marganska *et al.*, superconductivity is introduced by the presence of a thin layer of 2H-niobiumdiselenide (2H-$NbSe_2$, $NbSe_2$) [8] *. $NbSe_2$ is a superconducting transition metal dichalcogenide (TMD) having the trigonal prismatic (2H) phase. TMDs are layered materials of the type MX_2, where M represents the layer with the transition metal atoms and X the layer with the chalcogens. The structure of 2H-TMDs is determined by the stacking of triangularly arranged transition metal atoms (X) and chalcogen atoms (M): X-M-X, as shown in Fig. 2.5. The resulting lattice structure is the 2D hexagonal honeycomb lattice, similar to graphene [16].

Compared to the strong in-plane covalent bonds, the van der Waals bonds between adjacent stacks are much weaker. Due to this difference in bond strength, TMDs can be easily exfoliated in few layer thick quasi-2D crystals (cleave plane in fig 2.5). In this way, TMDs can be opened up down to an atomic monolayer, similar to graphene [17].

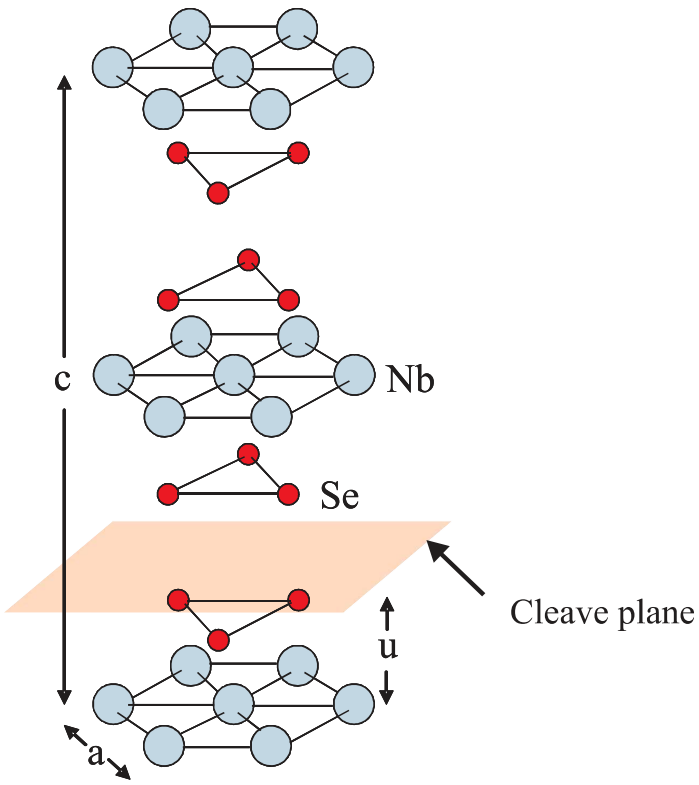

Figure 2.5: Unit cell of 2H-$NbSe_2$. The orange cleave plane represents the plane between the weaker van der Waals bonds that can be broken more easily than the covalent bonds between the three X-M-X layers. Distance between the two Nb planes is 6.3 $\AA$, the resulting c-axis thus has a length of 12.6 $\AA$. The a-axis has a length of 3.6 $\AA$ [17]. Figure adopted from Wang *et al. [18]*

In contrast to graphene, where the K and K' valleys are identical and represent degenerate states, states at the K and K' valleys in the hexagonal reciprocal lattice structure of few-layer

*In this thesis we are discussing the polytype 2H of $NbSe_2$ which we will indicate simply as $NbSe_2$ in the following

$NbSe_2$ are non-degenerate. This is due to the different environments of neighbouring atoms in the hexagonal lattice (A $\neq$ B) resulting in a broken sublattice symmetry [16].

This in-plane symmetry breaking and strong spin-orbit coupling result in a strong Zeeman field affecting electrons near the K and K' points [16]. Consequently, the spins of these electrons align according to the effective magnetic field (Zeeman spin-orbit field), which is directed out of plane and opposite for the K and K' valleys, hereby lifting the spin degeneracy. This out-of-plane locking of the spins oppositely for different valleys is referred to as spin valley locking, which is illustrated in Fig. 2.6a.

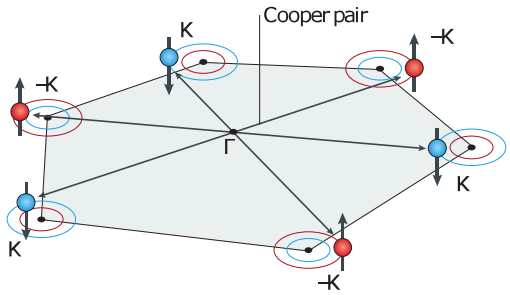

(a) Opposite spin polarizations for opposite valleys

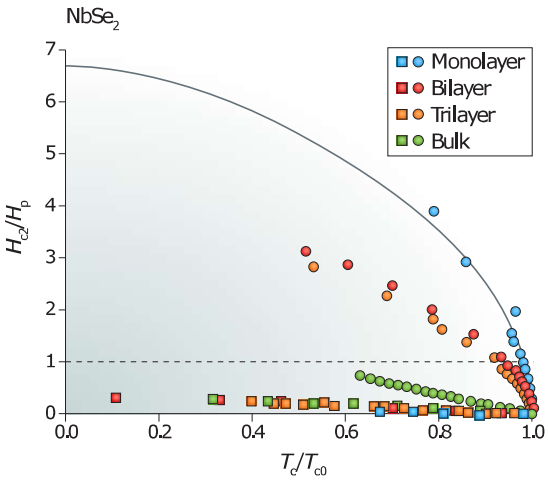

(b) $H_{c\|}$ enhancement [19]

Figure 2.6: Spin valley locking in $NbSe_2$ Figure (a) illustrates the spin-valley locking in the reciprocal space of monolayer $NbSe_2$. Figure (b) shows the $H_{c\|}$ enhancement measurement by Xi *et al.*. Dashed line in corresponds to the Pauli limit. Blue line fit for monolayer $NbSe_2$, predicts an upper parallel magnetic field of seven times more than the Pauli limit of $NbSe_2$, corresponding to an upper critical magnetic field of 31.5 T. Figures adopted from Saito *et al.*, 2016

$NbSe_2$ is a type II superconductor with a bulk critical temperature of 7.2 K [17] and a gap of 1.24 meV [8]. Although, layer dependent studies show a decrease in the critical temperature as the number of layers decreases, superconductivity persists down to the monolayer in $NbSe_2$.

The strong spin-valley locking for which the electron spins are forced out-of-plane, is found to enhance the parallel critical magnetic field $H_{c\|}$. In fact, in an ordinary 2D superconductor in parallel magnetic field superconductivity is destroyed for $H_{c\|}$ such that $E_{Zeeman} \approx \Delta_{SC}$. This is the so-called Pauli limit. However, if the spin is locked to the valley, then this limit can be violated. The enhancement of $H_{c\|}$ is shown in figure 2.6b, where the parallel upper critical magnetic field is plotted as a function of temperature for different layer thicknesses. This observation is confirmed in different experiments [19, 20]. From Fig. 2.6b, it is shown that monolayer $NbSe_2$ is predicted to sustain parallel magnetic field strengths of more than 7 times the Pauli limit, corresponding to a critical parallel magnetic field of about 31.5 T.

The ability to use atomically thin superconductors, allows tuning of the chemical potential inside the superconductor. Namely, the charge per unit area is low enough to be comparable to that of a parallel plate capacitor under reasonable voltage.

A recent experiment by Xi *et al.* 2016 on bilayer $NbSe_2$ [21], shows the possibility to tune the superconducting properties, such as the critical temperature, by means of electric double layer (EDL) gating (based on an ionic liquid). In this experiment, Xi *et al.* were able to change the carrier density by 30 % of the intrinsic charge carrier density. This change corresponds to an approximate 130 meV tuning range of the Fermi energy [21] and a 50 % variation of the critical temperature.

In the corresponding supplementary material Xi *et al.* report a comparison with a solid-state dielectric gate set-up [22]. The topgate consisted of few layer h-BN and graphene serving as the dielectric and gate contact respectively. Including the Si/SiO_2 backgate, only a < 4 % variation in the critical temperature was reached compared to a 50 % variation when using the ionic liquid [22]. This experiment shows the difficulty of significantly gating $NbSe_2$ with solid-state dielectrics and the advantage of using an ionic liquid.

2.2 Majorana modes in semiconducting carbon nanotubes

Above, we explained the main ingredients needed to reach the non-trivial topological phase in the semiconducting carbon nanotube hybrid device. The corresponding design as proposed by Marganska *et al.* is illustrated in Fig. 2.7a.

First, we have the one-dimensional carbon nanotube. The curvature induced spin-orbit coupling of the tube introduces a pairing term that couples between the nearest neighbour atoms, $t_{ij,ss'}$. This coupling is crucial to obtain the Majorana end modes in the wire. The spin-orbit coupling introduces a proportionality on momentum, creating an effective p-wave character in the s-wave $NbSe_2$ superconductor. As a result of the spin-orbit coupling, the bands are split for different spins resulting in a gap: Δ_{SO}. The resulting dispersion for a (12,4) semiconducting carbon nanotube is represented by the grey line plot in Fig. 2.7b. Because the states at $k = 0$ correspond to the different valleys and do not mix, the degeneracy at $k = 0$ remains. Therefore, even in the presence of a magnetic field, the dispersion does not show hybridization.

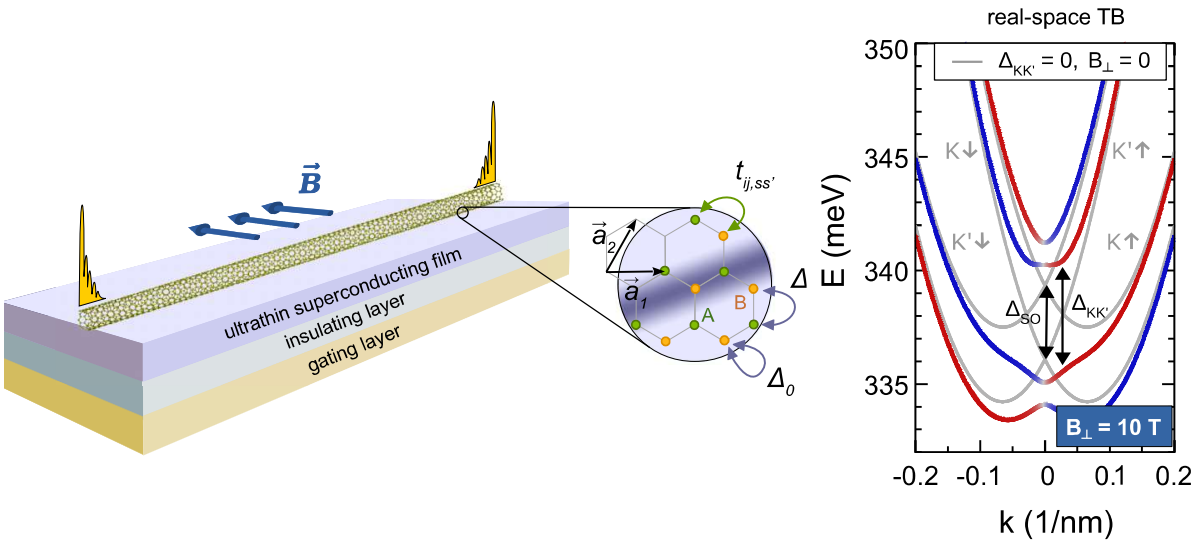

(a) Design **(b) Energy dispersion**

Figure 2.7: Design as proposed by Marganska et al. 2018 [8] A hybrid devices consisting of a gate tuneable superconductor (e.g. ultrathin $NbSe_2$) and a CNT is expected to host zero energy Majorana end modes for a certain magnetic field and gate range. This field must be perpendicular to the CNT's intrinsic spin-orbit interaction, which is along the wire axis. The inset shows the interactions at the interface of the carbon nanotube and the superconductor. As $NbSe_2$ lacks inversion symmetry (atom A $\neq$ atom B), its proximity to the tube will break the tube's rotational symmetry. The dark region represents the increase in electrostatic potential at the CNT - SC interface. Spin dependent hopping $t_{ij,ss'}$ is the result of spin-orbit coupling. Although nearest neighbour interaction (Δ_1) is allowed, the model takes into account the on-site superconducting pairing only (Δ_0). Figure (b) shows the corresponding energy dispersion of the hybrid tube. Spin-orbit coupling shifts the bands proportional to a finite momentum introducing: Δ_{SO}. The substrate removes the rotational symmetry of the carbon nanotube, allowing for the K,K' valleys to mix. Together with a magnetic field, the degeneracy at $k = 0$ is lifted: $\Delta_{KK'}$. Colors represent spin orientation.[8]

By adding a substrate, the rotational symmetry of the tube is broken allowing for the valleys to mix. Now, when we add this valley mixing $\Delta_{KK'}$, hybridization can take place in the presence of

a magnetic field that is orientated perpendicular to the spin-orbit field. The resulting dispersion of the normal state carbon nanotube in a magnetic field of 10 T is shown by the color line plot in Fig. 2.7b. The colors represent different spin orientations.

In case of a superconducting substrate, such as $NbSe_2$, superconducting pairing must be taken into account. The superconducting pairing ensures a electron-hole symmetric energy dispersion around the chemical potential. For a chemical potential of $\mu = 334.6\,\text{meV}$, the resulting superconducting spectra for different magnetic field strengths are plotted in Fig. 2.8. From these plots, it is shown that it is possible to obtain a non-trivial topological phase in the carbon nanotube - $NbSe_2$ device, from magnetic fields above 12.5 T. In this non-trivial phase, Majorana end modes appear at the edge. Here the edge is the boundary between the topological to the trivial phase, which is for this design at the boundary of the gate tuned $NbSe_2$ - carbon nanotube stack.

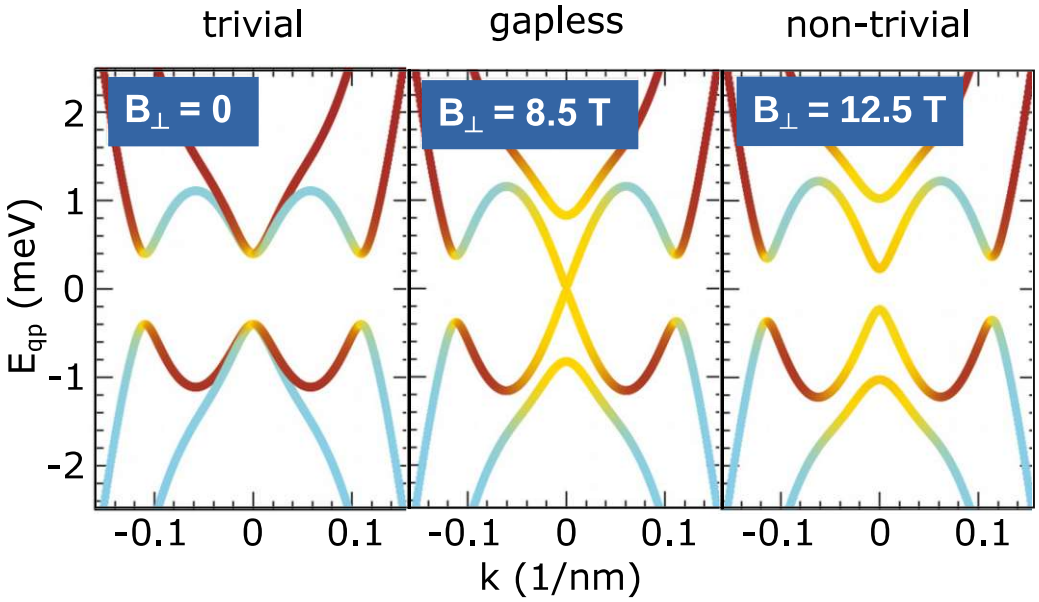

Figure 2.8: Superconducting energy dispersion hybrid device Superconductor imposes electron-hole symmetry. The result is that the energy dispersion is mirrored around the chemical potential of the $NbSe_2$. When this is tuned to $\mu = 334.6\,\text{meV}$, the following quasiparticle spectra can be obtained for different magnetic field strengths. At zero magnetic field, the system is in a trivial phase, due to the degeneracy at $k = 0$. $B = 8.5\,\text{T}$ represents the critical magnetic field above which at 12.5 T a non-trivial phase arises.

In order for superconductivity to persist at these high magnetic fields, the magnetic field must be applied parallel to the superconducting film. Due to the spin-valley locking in $NbSe_2$ discussed above, even the magnetic field necessary ($> 10\,\text{T}$) to reach non-trivial state does not break down the superconducting pairing.

Chapter 3

Device design and fabrication

In this chapter, the design and the corresponding work flow for the production of the hybrid carbon nanotube - $NbSe_2$ devices is described. In the fabrication section, we discuss in detail the mechanical exfoliation technique that is used to transfer the 2D materials to the sample and construct the hybrid device. First we start by describing the design of the device that determines the order of stamping flakes.

3.1 Design

In figure 3.1, a schematic overview of the device design is shown. The starting point is a carbon nanotube, on top of a $Si{+}{+}/SiO_2$ substrate (285 nm thermalized SiO_2). A thin, bi- or tri-layer, uniform $NbSe_2$ is positioned on top of the CNT. Source and drain contacts are connected at both ends of the proximitized tube. On top of the $NbSe_2$, a dielectric material and topgate are added in order for the proximitized tube to be gated locally. For a certain magnetic field and gate range, we expect the Majorana modes to appear for at the ends of the gate-tuned, proximitized region of the tube (*).

The separate layers are aligned such that they cover each other completely. The result is a uniformly gate tuned $NbSe_2$ over the region of interests. Aligning the stack in this way also enables to minimize the normal carbon nanotube lead length.

Figure 3.1: Hybrid device design. Uniform and thin $NbSe_2$ flake is stamped on top of the carbon nanotube. On the two sides of the $NbSe_2$ flake, a source and drain are connected to the carbon nanotube. On top of the $NbSe_2$ flake a stack of a dielectric material and a topgate is created. The topgate configuration allows for gate tuning of the superconductor. At the edges of the gate-tuned $NbSe_2$ the Majorana modes appear for a certain magnetic field and gate range.

CNTs are grown, by chemical vapour deposition (perfomed by Christian Bäuml), at tempera-

tures of about 900 K inside a steady flow of H_2 and CH_4 inside a quartz tube. At these high temperatures, materials such as $NbSe_2$ are destroyed. Therefore, CNTs must be grown in the first fabrication step.

3.1.1 h-BN as dielectric

Although electric double layer methods (EDL), have proven to be a very efficient way to electrostatically dope $NbSe_2$ by Xi *et al.* [21], the usage of an ionic liquid also has some drawbacks. As the gate value can be applied only in the liquid state, devices have to be warmed up every time the value of the gate is changed. This warming up is time consuming and might also be risky as contacts can break during too many cool downs. In order to allow for a more flexible experiment, we propose to use a dielectric material instead: h-BN. As a layered material, we can obtain thin layers of h-BN in the same way as exfoliating $NbSe_2$, which will be discussed below. Together with its high breakdown voltage, we expect to obtain a high breakdown field of about 1.2 V/nm [23] and a relative permittivity of at least 4, when combined with the gold topgate interface [24]. An optimistic expectation of the tuning range will then be 18 meV , which is less than the EDL method described by Xi *et al.*. However, when comparing with the calculated energy dispersion in Fig 2.6b, 18 meV seems like a sufficiently large tuning range, depending on the initial position of the Fermi energy.

Positioning of h-BN

From the design point of view however, mechanical exfoliation of the dielectric will always result in some uncertainty in the positioning of the h-BN with respect to the $NbSe_2$ flake, resulting in a deviation from the perfectly aligned stack as depicted in Fig. 3.1. In Fig. 3.2, two realistic implementations of the design are illustrated that show two different realizations together with the corresponding position of the Majorana modes.

(a) Complete $NbSe_2$ coverage **(b) Partial $NbSe_2$ coverage**

Figure 3.2: Experimentally realistic implementation design hybrid device Figure (a) shows a carbon nanotube covered by $NbSe_2$. The h-BN that is subsequently stamped on top of the stack is bigger than the $NbSe_2$ such that the stack can be covered completely. In this case, the topgate, that is fabricated by EBL, can cover the entire region where $NbSe_2$ covers the CNT. MFs appear at the edge of the gated region. Figure (b) shows a different implementation in which the h-BN flake is a bit smaller than the $NbSe_2$ region covering the CNT. In this case, the gating is not uniform over the entire superconducting region and MFs appear at the end of the gate tuned CNT-$NbSe_2$ region.

3.1.2 Magnetic field orientation

The magnetic field must be applied perpendicular to the wire axis but parallel to the $NbSe_2$. From SEM images taken after the nanotube growth, we can determine the orientation of the

CNT with respect to the markers on the chip. The chip has to be orientated inside the measuring set-up such that the CNT is within 5 degrees perpendicular to the applied magnetic field [8]. It is therefore preferable to select the straightest tube before stamping during the fabrication, such that the angle does not differ over the length of the CNT. Moreover, when the measuring set-up is equipped with of a rotator, one can define the stability of the modes as a function of magnetic field angle.

3.2 Fabrication

The fabrication of the proposed design can be divided in three main tasks, which can themselves be subdivided further:

- Preparation of isolated carbon nanotubes on Si/SiO_2 substrates (Illustration 1 Fig. 3.3)
- Exfoliation and stamping of the $NbSe_2$ and h-BN dielectric material and graphite contacts (Illustrations 2-4 Fig. 3.3)
- Electrically contacting the CNT and adding the topgate with Cr/Au contacts by electron beam lithography (EBL) and bonding to the puck (sample holder of the cryogenic measurement system). (Illustration 5 Fig. 3.3)

Specifically, the main task of this project is the exfoliation and the stamping which will be treated in detail. The other steps were done of by PhD candidate Christian Bäuml and are part of another project. For completeness, however, these steps will be briefly discussed in the appendix.

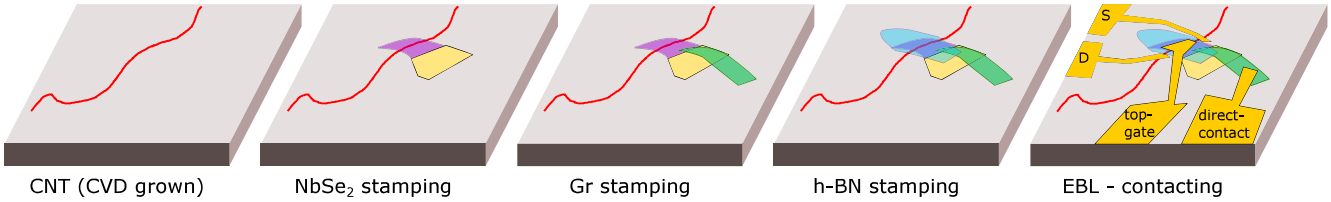

Figure 3.3: Overview fabrication process We receive substrates on which CNTs are grown. The thin part of an exfoliated $NbSe_2$ flake is stamped on top of the CNT. A long narrow graphite flake is used as a direct contact to the $NbSe_2$, as Cr/Au contacts do not work on $NbSe_2$ directly. After stamping the graphite, a thin h-BN flake with a shape that resembles the part of the $NbSe_2$ flake covering the CNT, is stamped on top of the stack. Finally, the CNT is contacted and a topgate is added by EBL and Cr/Au deposition.

3.2.1 Stamping environment

Previous research has shown that thin layers of $NbSe_2$ are unstable in ambient conditions [25]. For this reason, the exfolation and stamping of $NbSe_2$ is conducted in a home-built glove box. A constant nitrogen flow in the glove box reduces the concentration of oxygen to less than 100 ppm [26], in order to prevent oxidation of the $NbSe_2$ interface. Inside the glove-box, a stamping set-up (see Fig. 3.5), a hotplate and an additional optical microscope (with 4x, 20x and 100x magnification) are present.

3.2.2 Exfolation and flake identification

The optical microscope is used to search for the proper crystal flake. A proper $NbSe_2$ flake, is defined as a thin flake of at most 2 to 3 layers. In order to define a uniform gating field, a uniform thickness is, at least over the region of interest, which should overlap the CNT (by about 5 μm), necessary. However, often crystal flakes are found to have areas of different thickness. It is also important that the flake is isolated, i.e., not surround by bulky crystals. Searching for suitable isolated flakes of uniform thickness is currently the most time-consuming part of this technique.

In order to obtain such a flake and to be able to transfer it to substrate, we use an exfolation technique that is described in Fig. 3.4.

We start with a bulk crystal (2D semiconductors). A sticky 'white' tape is used to separate some material from the bulk crystal. The material facing the opposite site of the white tape, is newly opened and atomically clean. On this white tape, a lot of material is present which can be used for multiple stamping sessions, provided it is kept in a sealed jar which is permanently filled with N_2 and is opened only in the flow box. Secondly, a less sticky tape, the blue one, is used in order to open up the crystal further. We refer to this first blue tape as the first generation. In order to obtain isolated and bi or tri-layer $NbSe_2$ flakes, we repeat this two more times. Blue tapes sequentially open up the crystals on the previous blue tape. Finally, we end up with very little, but few-layered, material on the third generation blue tape.

At this point, we transfer some of the material on the blue tape to a small piece of polydimethylsiloxane film (PDMS) that is positioned near the edge of a glass slide. After transferring the material on the glass slide, we inspect the PDMS for flakes by means of the optical microscope inside the glove box.

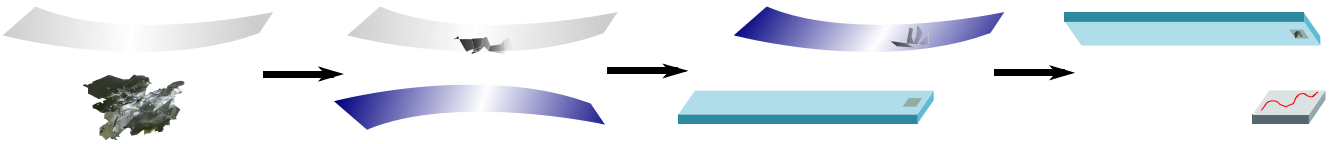

Figure 3.4: Stamping procedure A white tape is used to remove the top layer of a bulk crystal. This layer adheres to the white tape. Blue tape is then used to open up the material that adheres to the white tape. The resulting material on the blue tape is referred to as the first generation of an opened up crystal. One can open the crystal further by repeating this step with two blue tapes. The material on the third generation blue tapes is then transferred to a PDMS that is sticking to a glass slide. Finally, the crystals transferred to the PDMS are inspected under the optical microscope and in case of a proper crystal, the flake can be transferred to the substrate.

3.2.3 Stamping

Once the proper $NbSe_2$ flake is found, it can be stamped on top of the carbon nanotube. A SEM image, taken right after the growth, is used to identify the position of the tube with respect to markers present on the chip. The substrate is positioned underneath the zoomlens on top of a sample holder that is mounted on top of a piezo stack. A sticky tape ensures maximum adhesion to the sample holder. A non-sticky tape is used to induce an angle between the substrate

plane and glass slide plane, as can be seen from Fig. 3.5.

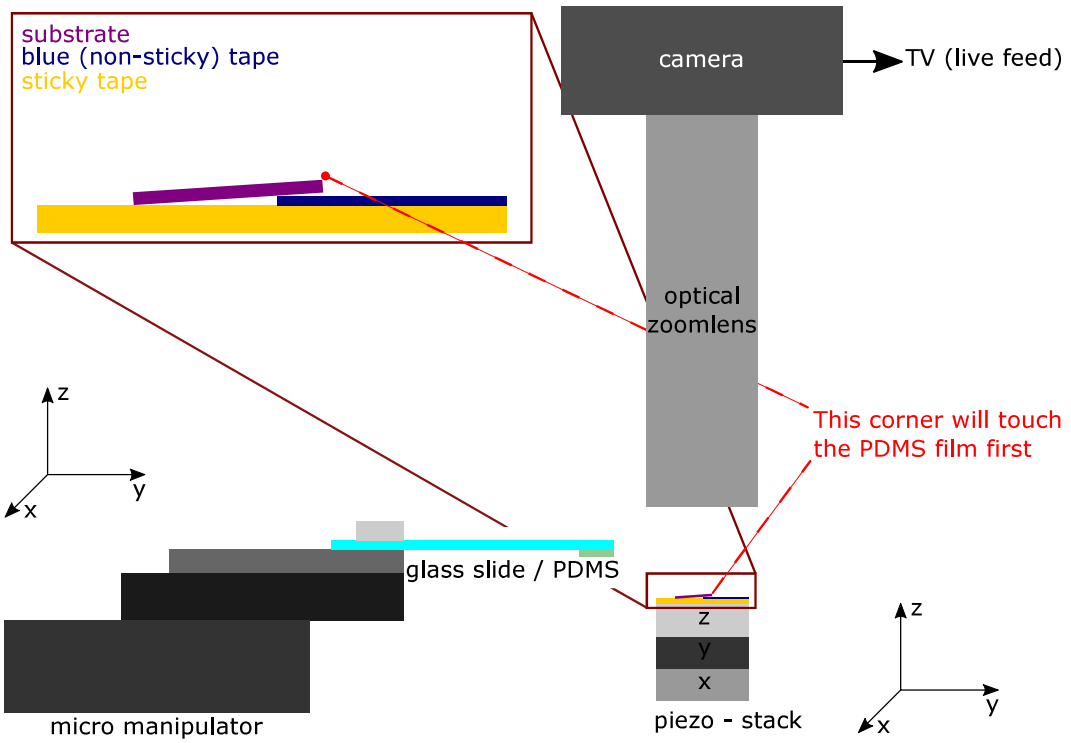

Figure 3.5: Schematic overview stamping set-up Micro-manipulator stage can be moved (by hand) around the piezo stack. The micromanipulators allow for a fine positioning of the glass slide with respect to the substrate. The piezo stack also allows for movements in three dimensions, allowing to change the position of the substrate. During the stamping, both the glass slide and the substrate can move towards each other. The optical zoomlens allows for a large working distance. A live feed from the camera is shown on a large TV screen allowing for a digital zoom. The substrate is mounted on a sticky tape. An extra blue tape enforces an angle between approaching PDMS and substrate, forcing the meniscus to come from above.

The glass slide containing the $NbSe_2$ flake is mounted upside down into the micromanipulator. By adjusting both the position of the micromanipulator by hand, by fine tuning with the micromanipulators and also by fine tuning the sample position with the piezo stack the optimum orientation of the tube versus flake is found. Now, the sample and glass slide can be moved towards each other, which is done either by moving down the glass slide with the micromanipulator or by increasing z of the piezo stack. Because of the angle with the sample holder, the sample will first touch the PDMS at its upstanding side (top). We continue with a sequence of small approaching steps followed by checking the position of the flake with respect to the chip. Once the PDMS has covered a significant part of the chip, changing the respective position becomes more difficult and more stress needs to be applied on the PDMS. This is unwanted, as it also induces some stress to the thin crystal. In case a major correction is needed, one can decide to retract the PDMS altogether and start the approach over. Once satisfied with the position of the flake, the PDMS can be lowered further until it completely covers the region of interest. Too limit the formation of trapped N_2 bubbles it is advisable to perform this step slowly. At this point, the $NbSe_2$ flake is in contact with the SiO_2 surface and the CNT. Usually the adhesion of $NbSe_2$ with the substrate is better than that with the PDMS, thus the $NbSe_2$ will likely remain

on the substrate after retracting the PDMS back. In case of bad adhesion, one can try to apply extra stress by sheering the PDMS in the x,y direction with the micromanipulators.

After stamping $NbSe_2$, we stamp a thin and small graphite flake (as in illustration 3 of fig. 3.3). This graphite flake serves as a direct contact to $NbSe_2$. From experience it is found that the normal Cr/Au contacts made in EBL do not contact $NbSe_2$, possibly due to the oxidation layer that follows from the EBL process. After the graphite stamping, we stamp the dielectric h-BN crystal. A flake is searched that matches the $NbSe_2$ flake shape. Moreover, the flake must be thin in order to obtain a sufficient capacitance per unit area for the gate. The difficulty in stamping h-BN, however, is the fact that optical contrast of the flake on the PDMS is extremely low. Without a reference point, it is very difficult to recognize a thin h-BN film under the zoomlens, which makes it difficult to align it with respect to the previously stamped $NbSe_2$ flake. Once the flake is in contact with the SiO_2, it is easy to recognize.

3.2.4 Annealing

After finishing the stamping of the hybrid device, the sample must be annealed (oven A600 MBE components). The annealing oven is first flushed with a mixture of nitrogen and argon (forming gas). Then the chamber is pumped down to 10 mbar. The flushing and pumping is repeated three times. At 10 mbar, the temperature is first ramped up until 150 °C in 390 s which then will hold stable for another 300 s. The temperature is then decreased to 30 °C in about 150 s and finally the chamber is vented and the sample is stored in vacuum while waiting for further processing (EBL and measurements).

Chapter 4

Experimental results

As the main task of the project is the design and fabrication of devices, we will focus in this chapter on a summary of the produced devices in order to show the improvement of the devices over time. Atomic Force Microscopy (AFM) images are taken in order to determine the position of the CNT with respect to the $NbSe_2$ and the h-BN flakes and to characterize the uniformity of the flakes in this region. In the second part, the results of the transport characterization of one of the first samples are shown.

4.1 Device summary

Figure 4.1 summarizes the fabricated devices that were made according to the first working strategy: We first stamped $NbSe_2$ (light purple) on top of the CNT (red). Secondly, a graphite contact (black) is added as a direct contact to the $NbSe_2$. Two more graphite contacts are added as the source and the drain on the left and right side of the CNT, as close as possible to the CNT-$NbSe_2$ stack. An h-BN flake is stamped to cover at least the CNT-$NbSe_2$ overlap region.

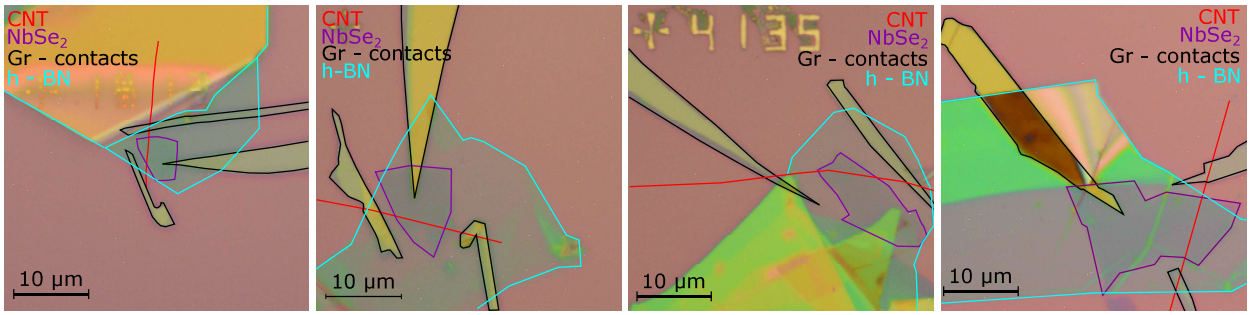

(a) CNT-128 **(b) CNT - 129** **(c) CNT-132** **(d) CNT-133**

Figure 4.1: Optical pictures early design devices Devices are fabricated by stamping a thin $NbSe_2$ flake on top of a CVD grown carbon nanotube. A direct contact to the $NbSe_2$ is stamped by means of a graphite contact. The source and drain contacts are added by stamping two additional graphite contacts next to the edges of the $NbSe_2$ carbon nanotube stack. Finally, an h-BN flake is stamped to cover the entire $NbSe_2$ and carbon nanotube stack.

In these figures, one can see that the h-BN flake covering the stack is always much larger than the width of the stack itself. When the h-BN is this large, it can have an arbitrary shape. This way also positioning the flake with respect to the device does not cost too much effort. This is illustrated in Fig. 4.2a. In this design, the topgate can be designed in such a way that it covers the entire CNT-$NbSe_2$ stack width as the h-BN protects the complete device from direct contact. This results in a proximitized tube that can be gate tuned almost along its entire length. The size of the carbon nanotube that is not gate tuned and proximitized to the source or drain acts as a normal lead to the hybrid stack. Important is to reduce this lead length, as transport in normal carbon nanotubes is often governed by quantum effects and disorder. The lead lengths, L_L and L_R, are for this design determined by the distance between the graphite contacts and the $NbSe_2$ flake.

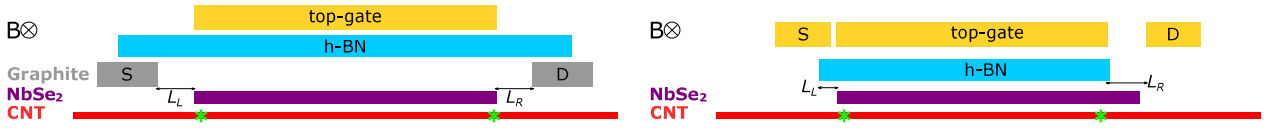

(a) Strategy I **(b) Strategy II**

Figure 4.2: Schematic overview working strategies Stamping order is from down to top (direct graphite contact to $NbSe_2$ not shown). Figure (a) illustrates the first stamping strategy. A carbon nanotube is covered by $NbSe_2$. Source and a drain contacts, in the form of two narrow graphite flakes, are stamped as close as possible to the edges of the CNT-$NbSe_2$ overlap region. This is in order to reduce the normal CNT lead length. As we have already stamped the two contacts, we can choose an h-BN flake of arbitrary size and shape, provided it covers at least the region of overlap of the CNT-$NbSe_2$ stack. Therefore a big h-BN flake can be chosen. As the h-BN safely covers the entire device, the topgate can be designed such that is nicely matches the width of the proximitized tube. MFs are expected to appear at the edge of the gate tuned proximitized CNT (*). Figure (b) illustrates the second working strategy. A $NbSe_2$ is stamped on top of a CNT. A h-BN is found with a shape that matches the width of the overlap region of the CNT-$NbSe_2$ stack. However, due to the low visibility of h-BN on the PDMS, the positioning of h-BN with respect to the CNT-$NbSe_2$ stack is difficult. Finally, source and drain contacts and topgate are fabricated by means of EBL. The stamping accuracy of the normal carbon nanotube lead length, is now determined by the parts where h-BN does not overlap the CNT-$NbSe_2$ stack, as indicated in the figure by L_L and L_R.

Although the former working strategy allows to produce working devices (see final section of this chapter), it happened that some samples were destroyed half way in the stamping procedure. Namely, every time a new flake is stamped on top of an existing stack, one risks to pick up previously stamped flakes with the PDMS.

In order to improve the success rate of the stamping sessions, the number of stamping steps was reduced for later devices. This also reduced the time needed to stamp a complete sample. Instead of adding the source and drain by stamping narrow graphite flakes, the source and drain were only fabricated after the stamping procedure by means of electron beam lithography (EBL) and Cr/Au deposition. The number of stamping steps is hereby reduced from five to three. Moreover, as the accuracy in EBL is much higher (nearly $0.1\,\mu$m) than the accuracy obtained by the micromanipulators and the piezo controllers in the stamping set-up (nearly $1.3 - 2.0\,\mu$m), these Cr/Au leads can be placed very close to the edges of the stack. In this new design, the lead size can be minimized when an h-BN flake is found that matches the width of the CNT-$NbSe_2$ overlap region and when it can be positioned accordingly. However, as mentioned before, positioning the h-BN with respect to the CNT-$NbSe_2$ stack is difficult, due

to its extremely low optical contrast on the PDMS. As the source and drain contacts can be positioned arbitrarily close to the edge of the stack, the normal carbon nanotube lead length is determined by the stamping accuracy of the h-BN with respect to the CNT-$NbSe_2$ stack. This is illustrated in Fig. 4.2b.

In Fig. 4.3, the devices that were produced according to the second working strategy are summarized.

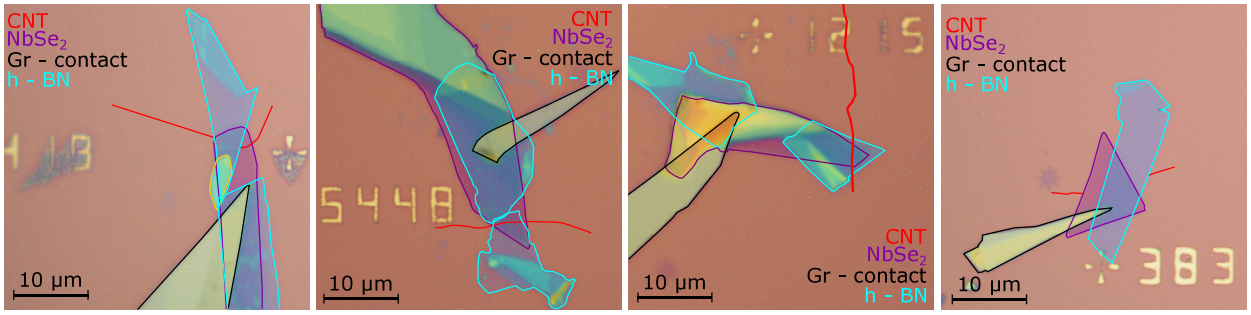

(a) CNT-142 **(b) CNT-143** **(c) CNT-145** **(d) CNT-146**

Figure 4.3: Optical images devices latest design Devices are fabricated by stamping a thin $NbSe_2$ on top of a CVD grown CNT. A graphite flake is stamped to serve as direct contact to the $NbSe_2$. Finally, a h-BN flake is exfoliated and stamped with a shape mathching the size and shape of the CNT-$NbSe_2$ stack. After stamping, source and drain contacts and the topgate are added by EBL and Cr/Au deposition.

4.2 AFM characterization

AFM images were taken on the devices that are summarized in Fig. 4.3 in order to determine the length of the normal CNT leads to the hybrid stack.

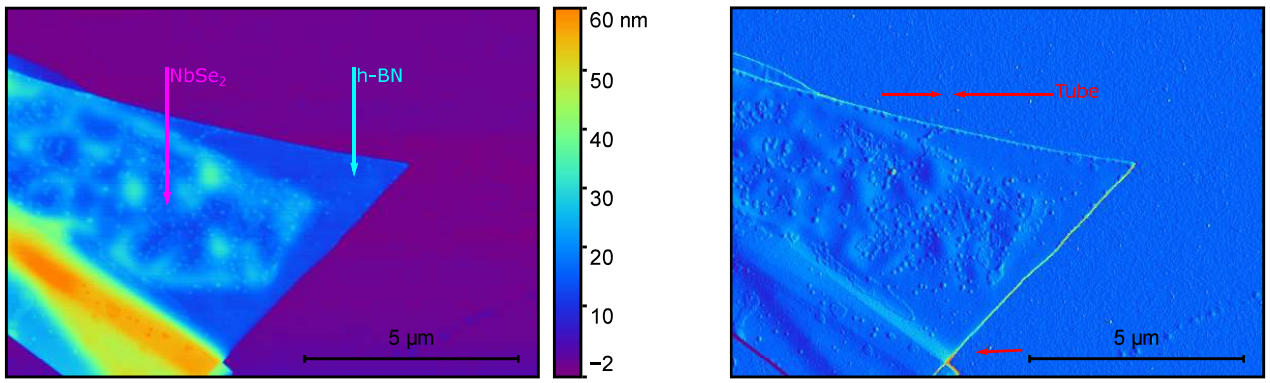

(a) Topography **(b) Phase**

Figure 4.4: AFM height and phase image CNT - 145 Height image shows the lower $NbSe_2$ layer, covered by a thin h-BN flake (flake with sharp corner). In this image, it is difficult to recognize the position of the tube, because of its small diameter. In the phase image, however, the position of the tube is recognizable and its position is pointed out by red arrows.

Figure 4.4 shows the topography and phase images of device CNT-145. We observe a smooth

substrate surface on which a $NbSe_2$ and a h-BN flake are stamped. The topography image in the region of the h-BN - substrate shows almost no irregularities, pointing at a clean interface. In the region with $NbSe_2$, however, bubbles appear. While stamping $NbSe_2$, we found that at the interface of the SiO_2 and the $NbSe_2$ bubbles are formed. As samples are stamped in a nitrogen environment, air can be excluded as the origin of these bubbles. Instead, we suspect that a water layer is formed on the $NbSe_2$ surface after transferring it to the PDMS. A more extensive study on the behaviour of these bubbles is reported in the Bachelor thesis of Andrea Seitz (2018) [27]. These bubbles might become problematic when ensuring a good contact between the CNT and the $NbSe_2$ which should be uniform over the entire length of the carbon nanotube - $NbSe_2$ stack. However, maybe this uniformity is not so critical, theoreticians say.

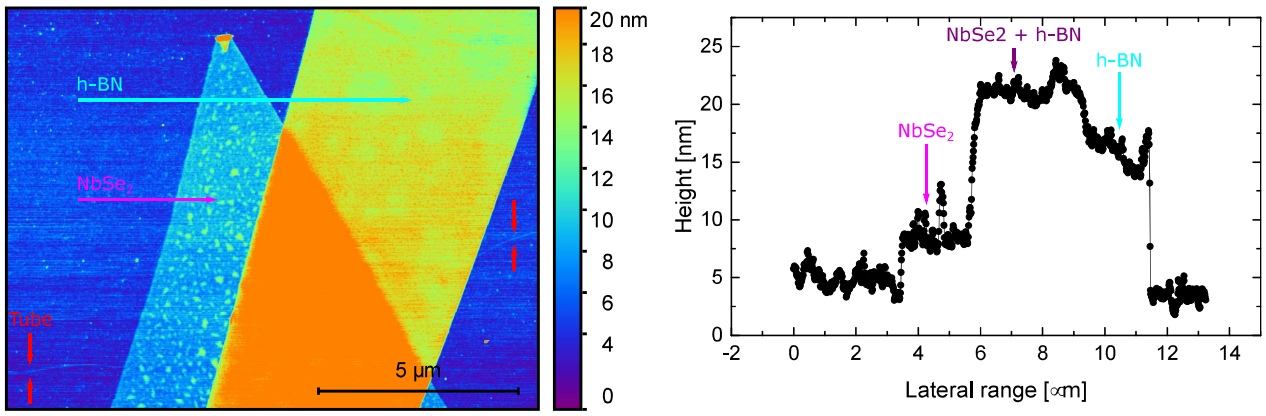

(a) Height **(b) Trace**

Figure 4.5: AFM height image CNT - 146 with corresponding trace From the height image bubbles are observed in $NbSe_2$. From the trace we can estimate the layer thickness to be approximately 6 nm for $NbSe_2$ and 13,nm for h-BN.

From the AFM trace in Fig. 4.5b, we can estimate the thickness of the flakes. A thickness of 6 nm is measured for $NbSe_2$. From this value we could conclude that we are dealing with a very thick $NbSe_2$ flake. However, from a comparison with Raman spectroscopy measurement AFM is known to overestimate the thickness of the first layer [27]. Rather than to rely on AFM images only, we use the optical picture to define an estimate of the thickness. From the color of the flakes with respect to the SiO_2 color, we estimate that the flake consists of three layers. The thickness of the h-BN is estimated to be 13 nm.

In table 4.1, the lead sizes to the hybrid devices are listed. For the first four samples, we estimate the size by comparing the position of the CNT from the SEM image taken right after CNT growth with the optical picture after the stamping. From the table, we observe that a minimum lead size of about a micrometer can be obtained. However, this is only obtained for one out of the four devices. The last four devices, fabricated in the latter working strategy have lead sizes that are smaller on average. From this we can conclude, that even with the difficulty of the h-BN positioning one is still able to get a relatively good aligned CNT-$NbSe_2$-hBN stack. The last four lead sizes have been determined by AFM.

Sample	L_L	L_R	Length estimation method
CNT - 128	3.2 μm	0.9 μm	Optical / SEM image comparison
CNT - 129	1.3 μm	2.0 μm	
CNT - 132	5.5 μm	4.1 μm	
CNT - 133	2.3 μm	2.2 μm	
CNT - 142	1.6 μm	0.2 μm	AFM
CNT - 143	2.5 μm	2.5 μm	
CNT - 145	1.1 μm	0.8 μm	
CNT - 146	0.3 μm	1.0 μm	

Table 4.1: Stamping accuracy metallic leads Lead sizes of the first four devices are determined by a comparison between the original SEM images taken right after the CNT growth and the optical picture after stamping. For the final four devices, AFM images are taken as they give a higher accuracy of the exact lead length.

4.2.1 Carbon nanotube pick up

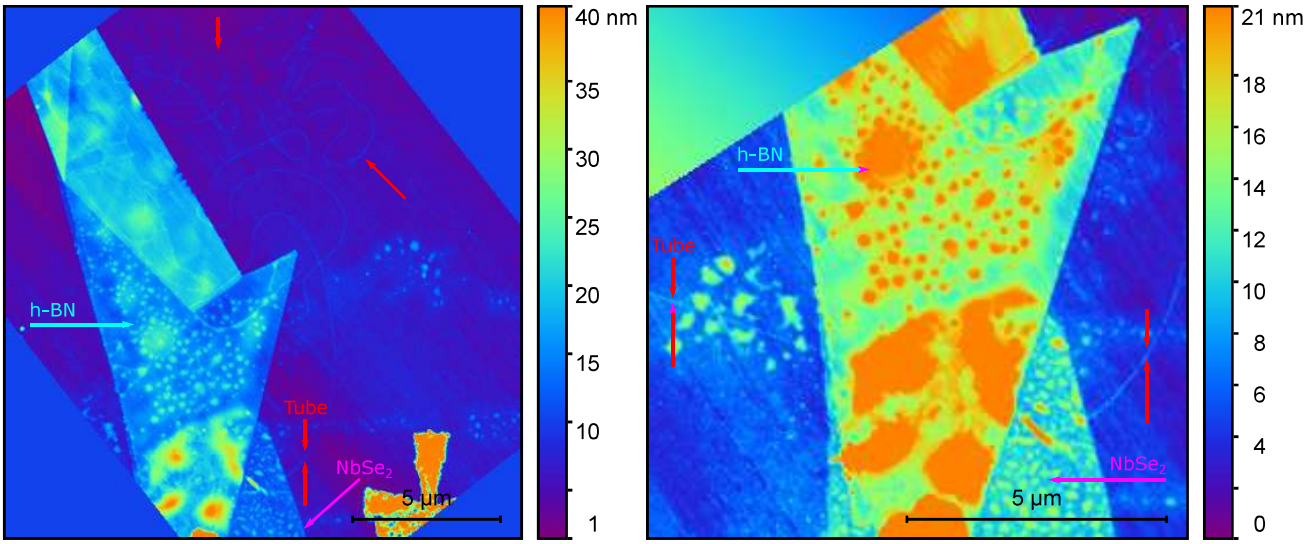

(a) Topography **(b) Topography**

Figure 4.6: AFM height images of CNT - 142 AFM images of the device after stamping show a displacement of the tube. Tube enters device straight on the left side, but on the right side the tube is curled up as a spring. Replacement of tube most probably occured during the stamping of $NbSe_2$ during which often a lot of stress is necessary in order to adhere to the substrate. The stress of the PDMS on the substrate results in a picking up of the tube. The bends in the tube are most likely due to the multiple stamping attempts and represent a PDMS that is being retracted and pushed down multiple times before being retracted completely.

It is found empirically that the hBN top layer is not perfectly air tight. Therefore to minimize exposure to O_2 it is necessary to process the stamped samples directly after stamping, or to store the samples in vacuum. However, after stamping a batch of samples, it was found that in some cases the leads were no longer connected. Although in smooth stamping processes the tube almost always remains on the substrate, when a lot of stress is involved in the stamping

process it might happen that the PDMS or a flake that has been stamped on top of the CNT, picks up the CNT.

In order to prevent wasting unnecessary EBL processing steps we decided to implement an extra AFM session directly after the stamping procedure. AFM was chosen over scanning electron microscopy in order to reduce the $NbSe_2$ exposure to high energy electrons. From Fig. 4.6, the necessity to perform AFM after stamping is obvious. In this device, the original tube was a straight tube. During the stamping of the $NbSe_2$, the adhesion of the $NbSe_2$ to the substrate was not high enough and a lot of stress was applied in order to make the flake adhere to the surface. The bends in the tube, show the many stamping attempts in which we tried to retract: meniscus is forced up and down until adhesion of the $NbSe_2$ is observed.

4.3 Transport characterization of sample CNT-128

In this section, we show the results of the transport characterization of one of the first produced samples: CNT-128. Data was received by Christian Bäuml, who conducted the transport measurements. Measurements were conducted in two different systems: the 2 K - stick, a cryostat that can cool down to 2 K and an Oxford He-3 system, which can cool down to 300 mK and in which a magnetic field can be applied.

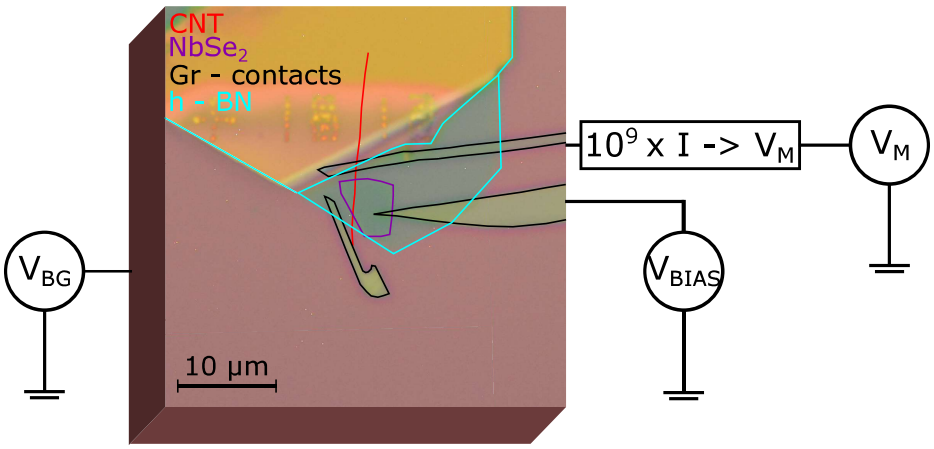

Figure 4.7: Measurement scheme CNT - 128 A bias voltage is applied between the middle graphite, the $NbSe_2$ flake, the proximitized part of the carbon nanotube, the normal carbon nanotube and finally the right graphite contact. The resulting current is amplified and converted into a voltage that is measured with a multimeter. The Si/SiO_2 substrate serves as a gate/dielectric in order to be used in a backgate configuration. The left graphite contact is not working as it is not connected to the tube. The topgate, that is produced in the final EBL step, is not shown in this picture.

Figure 4.7 shows an optical image of CNT-128 before the EBL procedure. The topgate, that is fabricated on top of the CNT- $NbSe_2$-h-BN stack is therefore not shown in the illustration. As a first characterization, we leave out the usage of the topgate and use a global backgate configuration instead. The Si^{++}/SiO_2 substrate here serves as the backgate contact and the dielectric respectively. This gate will mainly act on the part of the devices that is not screened by $NbSe_2$ in its superconducting state. Silver paint is used to connect the backgate to the sample holder connections.

A bias voltage is applied between the middle graphite, the $NbSe_2$, the proximitized carbon nanotube, then the normal carbon nanotube and finally the right graphite contact. The resulting current is converted into a voltage by a current voltage amplifier.

In this set-up the left graphite contact is not in use, as after the EBL process it was found that is was not connected to the carbon nanotube.

First, we show in Fig. 4.8 a conductance measurement over a large range of backgate voltages in the low bias regime. The conductance is measured both at room temperature as well as at a low temperature of 4.2 K. In the negative gate regime, where transport is mediated by holes, the conductance is much higher than in the electron transport regime, as usual in CNT devices. Moreover, we observe that the gap is not symmetric around zero.

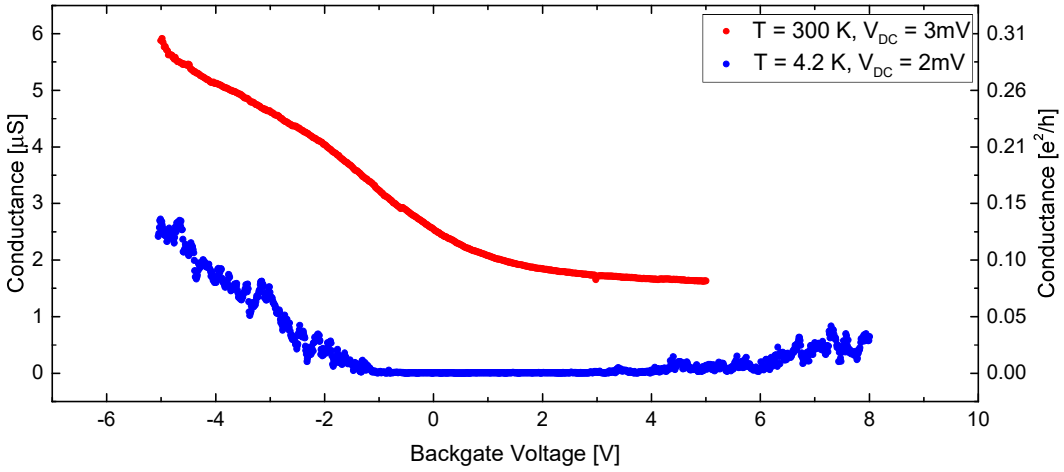

Figure 4.8: Conductance for large range of backgate voltages at low bias at room temperature and at 4.2 K Measurement conducted in 2-K system. Conductance is much higher in the hole transport regime regime than in the electron transport regime. An anti-symmetric gap is visible around zero backgate voltage.

Following the gate sweep, two stability diagrams were measured both in the electron transport regime (Fig. 4.9) as in the hole transport regime (Fig. 4.10). In these diagrams, we plot the conductance as function of bias and backgate voltage. The conductance was obtained by measuring single current-bias curves for each value of the backgate voltage.

Both diagrams show diamond shaped structures that are characteristic for transport in CNT quantum dots. The diamond structures are a result of Coulomb blockade inside the CNT. This can be described by a small conductive island (the CNT) that is confined by two isolating regions that arise at the interface with the measuring leads. Inside the island, the chemical potential takes discrete values depending on the number of electrons. This so-called quantum dot has a capacitance C. The corresponding charging energy: $E = e^2/C$, determines the spacing of the different values of the chemical potential. By means of a gate, the values of the chemical potential can be shifted up an down electrostatically. A bias window is defined by the chemical potential between the source and drain. When the chemical potential of the dot lies inside this bias window transport occurs.

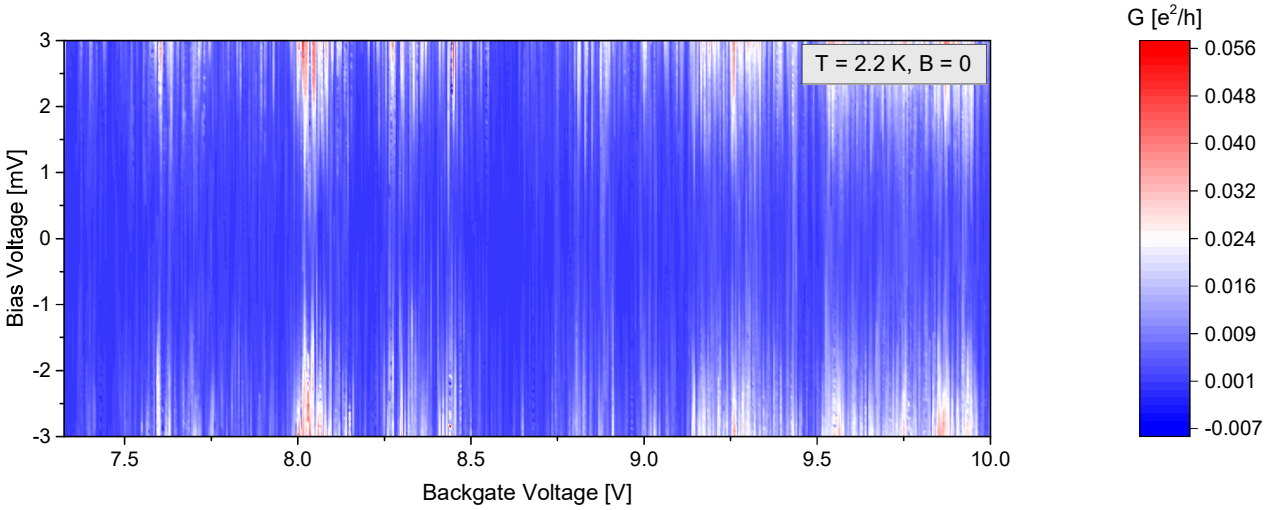

Figure 4.9: Stability diagram electron regime Measurement conducted in the 2-K system. Large backgate range, many big dots are visible. Inside these bigger dots, smaller dots seem to be present.

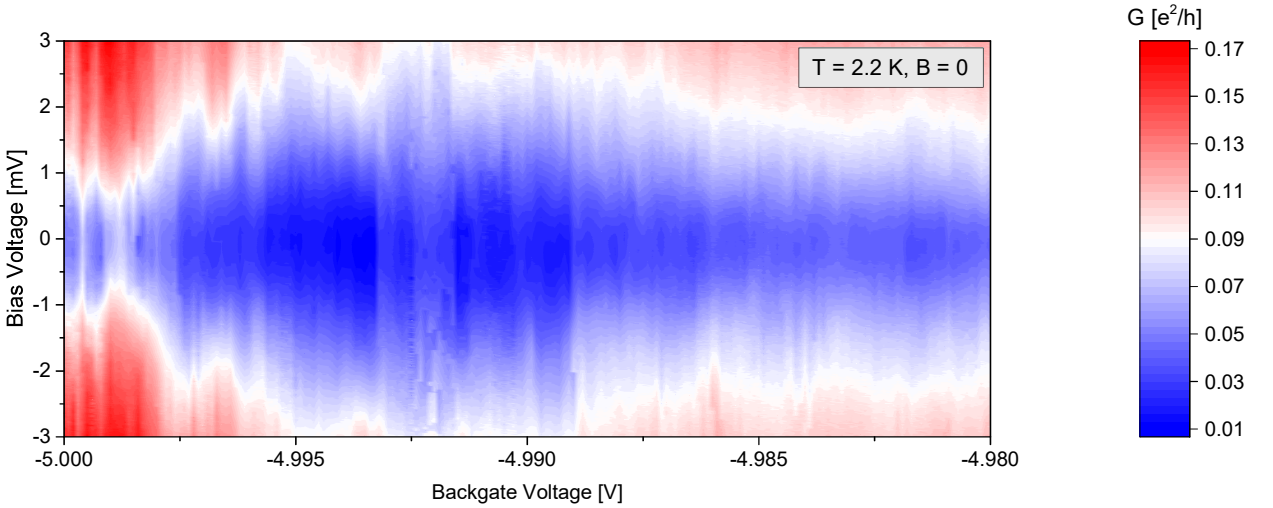

Figure 4.10: Stability diagram hole regime Measurement conducted in the 2-K system. High resolution backgate voltage range in the hole transport region. Stability diagram resolves a big diamond. In contrast to the diamonds measured in ultra clean CNTs [28], this diamond also has additional structures inside the diamond.

When the conductance is measured in ultra clean carbon nanotubes over a small length one finds diamonds that are sharp and close at zero bias [28]. Our stability diagrams however, show a much more complex behaviour as a function gate voltage. The stack of different materials, the CNT-$NbSe_2$ combination, very likely introduces the complex behaviour. Although at 2.2 Kelvin the $NbSe_2$ is deep in its superconducting state, we have not distinguished any unambiguous superconducting features in these diagrams yet. Besides, the relatively long length of the CNT over which the conductance is measured might suggest that the resulting spectrum is due to multiple dots in series.

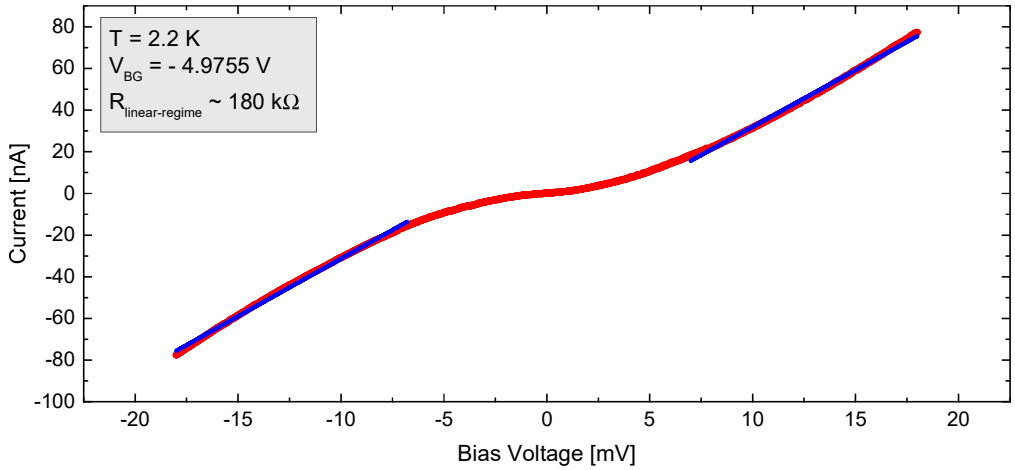

Figure 4.11: Current measurement for high bias range. Blue line represents the two linear fits in both the negative as both the positive bias regime. From these fits, the resistance is determined to be: $\approx 180\,\mathrm{k}\Omega$ both for negative as for positive bias.

Figure 4.11, shows the current as a function of voltage bias over a high bias range. At a backgate voltage of V$= -4.9775\,$V is chosen, a regime in which the conductance is relatively high. A linear fit reveals a resistance of about $180\,\mathrm{k}\Omega$, which is considerably less than the $\approx 25\,\mathrm{M}\Omega$, measured in an earlier device reported by Bauriedl and Bäuml [29].

4.3.1 Magnetic field dependence

The complicated diamond structures discussed above show that there is a gap that (almost) never closes as a function of gate voltage. Magnetic field dependent studies were conducted in order to observe a sign of superconductivity, e.g. a superconducting gap that disappears as a function of magnetic field. The results of this magnetic field dependent study are summarized below.

In Fig. 4.12, stability diagrams for different fields and temperatures in the high conduction regime of the backgate voltage are compared. As 4.2 K is below the transition temperature, $NbSe_2$ is superconducting in the top graphs. However, as it is not far away from the transition temperature, one can expect that the superconducting state is not as state strong as for 300 mK, for which the system is deep in the superconducting state. Moreover, at higher temperatures the diamond features are expected to be smeared out, as thermal excitations become more prominent compared to the charging energy associated with Coulomb blockade.

We observe that when lowering the temperature, we reach a state in which the gap never closes. A comparison with the stability diagram at 5 T however, shows that even at these high perpendicular fields the gap does not close. Although there is some change in the diagrams for different magnetic fields, a sign of superconductivity is not apparent.

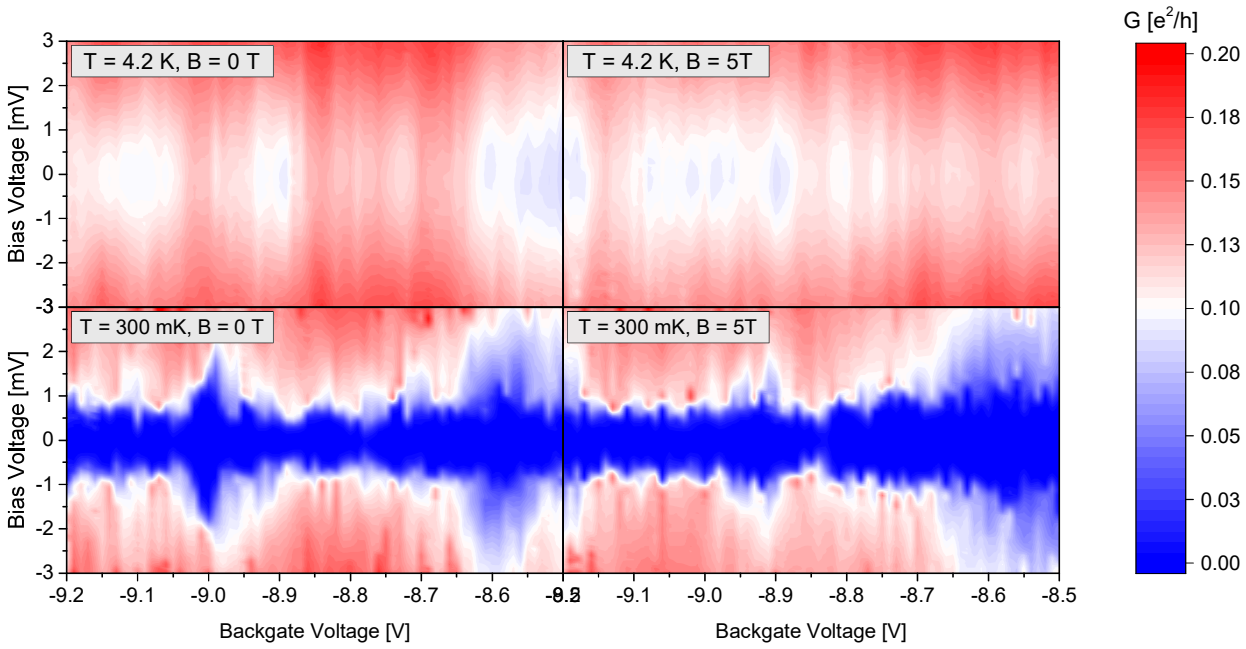

Figure 4.12: Stability diagram comparison, for field and temperature Same color range is used for all four graphs. In the 4.2 K measurements, the overall conductance is higher than in the 300 mK regime. At the lower temperatures a gap is visible that does not close at a high magnetic field of 5 T.

For completeness, we show a similar comparison at 300 mK in a different gating regime in Fig. 4.13. In this regime, the overall conductance is lower, so a smaller color range is used than for the comparison in figure 4.12. Although again the gap never closes, in this gate range, is it clear the the gap becomes smaller for higher fields. Since the gap survives at such high magnetic fields, it must be, then caused by something else than superconductivity.

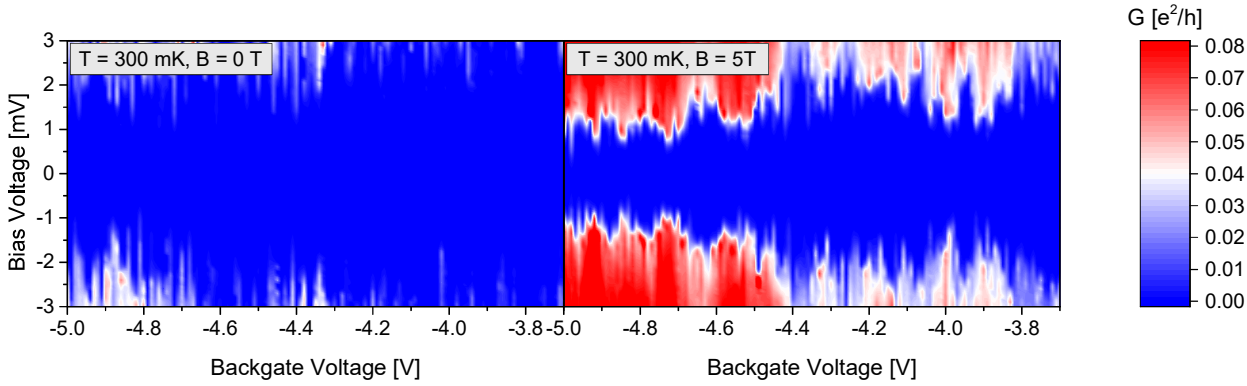

Figure 4.13: Stability diagram -5 V gating regime. Figure shows magnetic field comparison of two stability diagrams in different gating regime at the same temperature. Current is measured in the same bias voltage window as well as backgate voltage window. Same color range is used for both diamonds, however note that the color range is much smaller than in Fig. 4.12

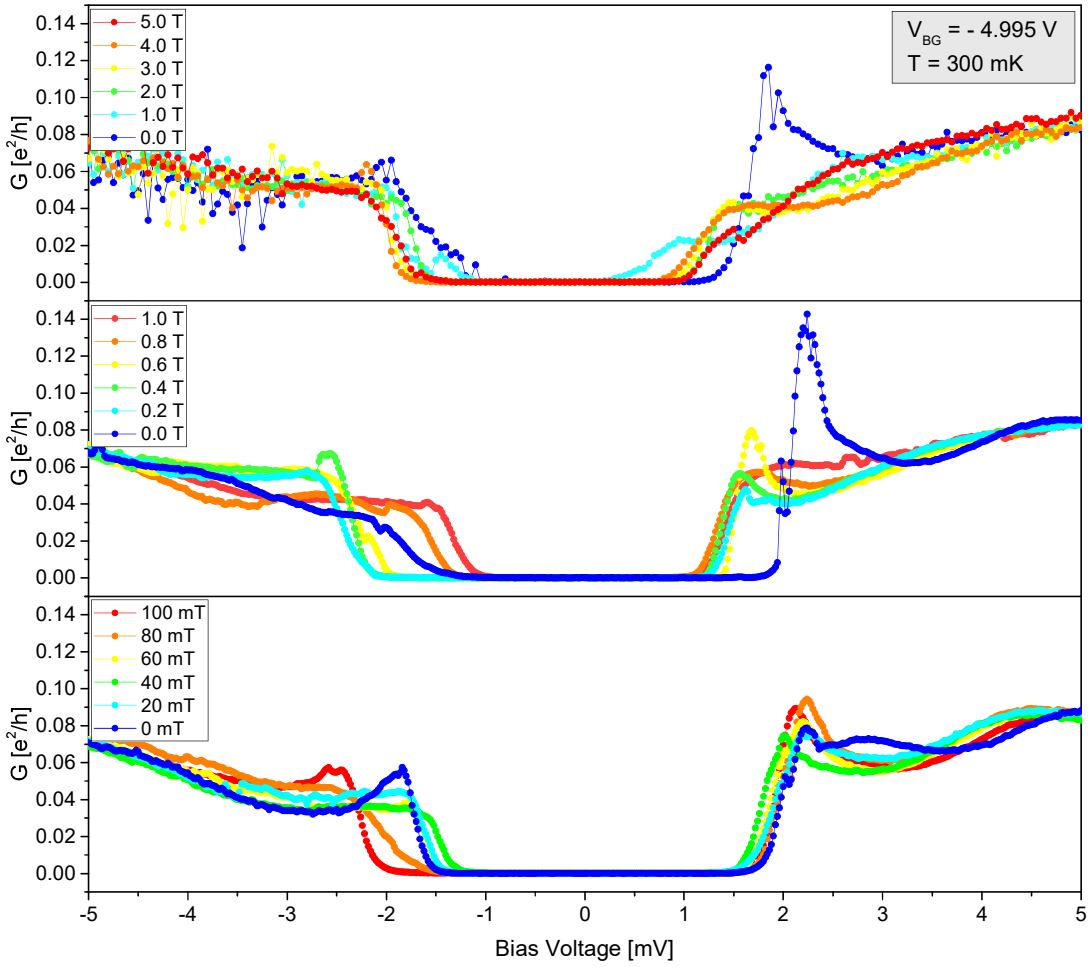

Figure 4.14: Magnetic field dependence of the conductance traces In this measurement, the magnetic field is gradually lowered from 5 T to 0 T in the top graph, from 1 T to 0 T in the middle graph and from 100 mT to 0 mT in the lower graph at a constant gate voltage.

Figure 4.14 shows a magnetic field dependent study of the conductance at a constant gate voltage of V= −4.995 V. For each graph, the magnetic field is gradually reduced to zero field. The top graph, shows the evolution of the conductance from 5 T to 0 T. At zero magnetic field, a peak in the conductance very much resembles the peak observed in the density of states in a superconductor. But, although this peak disappears for higher magnetic fields, the gap never closes. Even at 5 Tesla, still a gap is present. Although the gap is of similar strength as the superconducting gap in $NbSe_2$ (about 1 meV [8]), the gap in these graphs is therefore not caused by superconductivity. Moreover, as we study the high conductance peak for smaller magnetic field steps in the lower graphs, we observe an oscillating behaviour in the strength of this peak as a function of magnetic field instead of a gradual decrease.

A closer look on the gap sizes shows a decrease of the gap size as a function of magnetic field. Another observation is that the offset from zero bias changes for each curve.

4.3.2 Break down field topgate

In order to gate tune the $NbSe_2$ significantly, a strong electric field must be applied. As h-BN can be exfoliated down to few layers easily, the applied electric fields can become very large. However, there is a limit to the maximum applicable field. Namely, above a certain electric field strength, an irreversible breakdown of the dielectric occurs. This results in leaking currents. In Fig. 4.15, we observe a change in the sign of the current above a field strength of about 8 V as a result of the negative leakage with respect to the positive current from the bias voltage. This negative current clearly comes from the topgate. Following measurements also show that the previously applied field strength resulted in an irreversible breakdown of the h-BN.

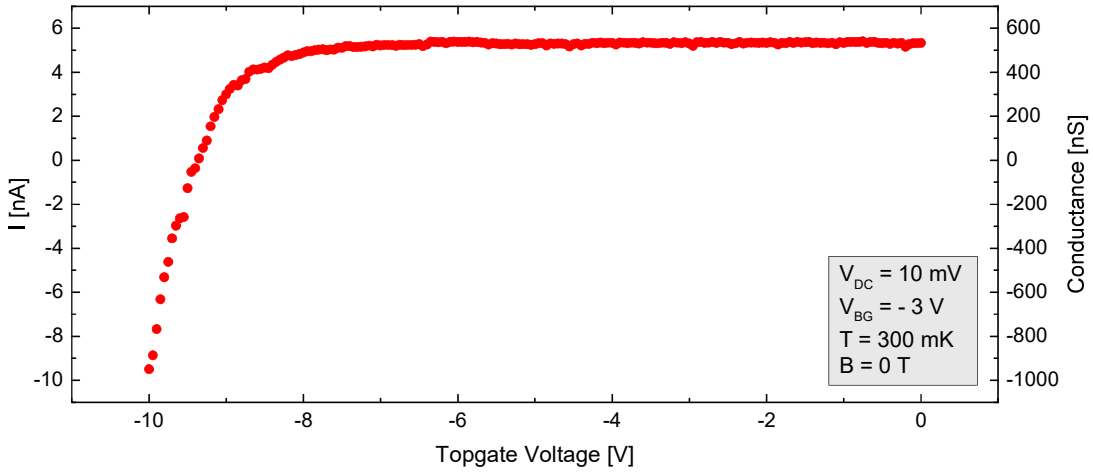

Figure 4.15: Break down field topgate configuration determination Current is measurement as a function of topgate voltage at a constant backgate voltage and bias voltage. An irreversible breakdown of the dielectric occurs for gate voltages below V$= -8$ V.

Although, an exact measurement of the h-BN thickness is not available the thickness is estimated to be about 10 nm from a comparison of optical pictures and AFM measurements on similar devices. The electric breakdown field is thus: 0.8 V/nm, which is on the same order as expected from Hattori *et al.*, 2015 [23]. Taking into account a relative permittivity of at least 4 [24], we expect to induce a change in charge carrier density of:

$$\Delta n_{2D} = \frac{\varepsilon_0 \varepsilon_R}{e} E = 1.8 \cdot 10^{13} \mathrm{cm}^{-2} \tag{4.1}$$

Comparing this with recent experiments of Xi *et al.*, a field of 0.8 V/nm allows us to tune the chemical potential by about 12 meV. From the bandstructure calculations of Marganska *et al.* in Fig. 2.6b, a range of about 12 meV can be sufficient in order to tune the chemical potential significantly. This is provided that the Fermi energy is located near the bottom of the conduction band of the hybrid device (or near the top of the valence band).

Chapter 5

Conclusion

This work has shown the ability to produce CNT-$NbSe_2$ hybrid devices in a reliable way by mechanical exfoliation. Producing a complete device was shown to take no longer than half a day of preparation and a single day of stamping. In this day, the device was kept in inert atmosphere during the entire stamping process, hereby minimizing the risk of exposure to air. AFM images show that a lateral stamping resolution of about 1 μm can be obtained of the carbon nanotube lead size to the hybrid device. AFM images, however, also show that bubbles appear underneath the thin $NbSe_2$ stamped layers.

The present work continuous and develops the work of C. Bäuml and L. Bauriedl who produced the first proof-of-principle device. Our work aimed at producing devices already in the final form required by the proposal of Marganska *et al.* [8]. Also, we moved the fabrication process into the glove-box. As a result, we have improved the conductance of the first proof-of-principle device by more than two orders of magnitude.

The origin of the gap in the differential conductance is, however, not yet completely understood. Both the stability diagrams as a field evolution study show complex behaviour that can not immediately be explained in terms of an ultra clean proximitized carbon nanotube. As a batch of similar samples has already been fabricated, the origin of this gap can be investigated further in the next transport measurements. Moreover, the breakdown field of the topgate configuration is found to be high and it might be sufficient to significantly gate tune the $NbSe_2$ electrostatically, depending on the initial position of the Fermi level.

In order to conduct the final Majorana Fermion detection experiment as proposed by Marganska *et al.* 2018 [8], a spectroscopy measurement must be conducted in a field that is with 5° of acceptable error margin. Future experiments will therefore also have to include the alignment of the tube to the magnetic field direction. Another point of improvement is the carbon nanotube $NbSe_2$ interface. Bubbles that arise between the Si/SiO_2 $NbSe_2$ interface might be reduced by stamping $NbSe_2$ on top of h-BN. In order to do so, carbon nanotubes must be grown on top of h-BN directly. Although this is experimentally possible [28], it is an extra time-consuming step in the fabrication process.

Acknowledgements

I would like to use this opportunity to acknowledge a few people that were crucial for the realization of this thesis and the corresponding research. First of all, I would like to express my deepest gratitude to my direct supervisor Dr. Nicola Paradiso from Regensburg University. I want to thank him for the time he took to explain and discuss many of the complicated subjects we were dealing with. But most of all I want to thank him for guiding me through the project and advising me.

Secondly, I wish to express my sincere gratitude to Prof. Dr. Christoph Strunk for giving me the opportunity to work in his group and invite me to the university of Regensburg. It was a great experience to be able to work in the Strunk Arbeitsgruppe among many interesting and very kind people.

I want to thank Christian Bäuml for working together on this interesting project making it possible to obtain so many results in such a short time. I also want to thank him for allowing me use the results from the transport measurements and his help.

I wish to thank Anh-Tuan N-guyen for his patience in introducing me to how to become a good stamper and his excellent explanations. I would also like to thank Sofia Blanter for her advice and sharing her experience on mechanical exfolation.

I thank Andrea Seitz for working together on many shared topics and also for introducing me to the real culture of Bayern and her friends, making my experience in Regensburg complete.

Finally I would like to thank Prof. Dr. Jan Aarts for introducing me to the Strunk Arbeitsgruppe and I would like to thank Prof. Dr. Ir. Tjerk H. Oosterkamp for taking the time to read and comment the thesis.

Appendix A

Fabrication: CNT growth and electron beam lithography

In this chapter, fabrication steps that were not part of the project, but are necessary to complete the devices are explained. These steps were performed by PhD candidate Christian Bäuml. The steps include the preparation of the CNT substrates before the stamping procedure and the metallization of the devices including the electron beam lithography (EBL) and chromium/gold deposition after the stamping are discussed.

A.1 Preparation CNT substrates

Substrates for the device are doped silicon (Si++) wafers covered with 285 nm of thermalized SiO_2.

Before the CNTs can be grown on top of the substrate, markers are created by means of EBL and chromium/gold deposition. These markers represent a coordinate system. In this step, an electron sensitive resist is spin coated on top of the substrate. During the EBL, the resist is exposed in a specified design. The polymer bonds in the exposed region have become weaker due to interactions with the electrons. By developing the resist after exposure, the weak polymer bonds are removed and the unexposed parts remain as a mask. After developing the resist, a thin film of chromium ($\sim$ 3 nm) serving as the sticking layer and gold ($\sim$ 40 nm) layer are deposited on top of the mask. Finally, the resist mask is removed by the lift-off method: the substrate is kept in acetone for at least an hour in order to remove the resist layer. The result is a chromium/gold structure on top of the Si/SiO_2 substrate.

After the marker fabrication, another EBL step is necessary in order to create catalyst dots from which the carbon nanotubes can start growing. In Fig. A.1a, an example of such a catalyst dot is shown. The catalyst dots are created in the same way as the gold markers, but instead of chromium/gold are made of cobalt.

Finally the carbon nanotubes are grown using chemical vapour deposition (CVD). In this technique, the substrates with the catalyst dots are transferred to the center of a long quartz glass

tube which is positioned horizontally. Inside the tube, carbon residues are present. First the tube is flushed with all gasses necessary for the tube growth (Ar, CH_4, Ar). After closing the CH_4 and H_2 gas valves, the temperature of the oven surrounding the tube is set to 900 °C in a steady flow of the inert gas Argon. When the temperature is reached, the CH_4 and H_2 valves are opened. The Ar flow is set to zero. The resulting gas stream is providing the carbon. As a result, the tubes start growing from a catalyst dot or some other cobalt residue in vertical direction, perpendicular to the surface. After reaching a certain height, the tubes fall down to the surface, often in the direction of the gas stream (along the tube). The process is very sensitive to changes and must therefore be altered for new situations. After some time, typically 20 min, the CH_4 and H_2 flow is stopped, and in the presence of Ar gas, the sample is cooled down to room temperature. Finally, the sample can be taken out of the inert atmosphere.

As a last step, scanning electron microscopy (SEM) images are taken in order to identify the position of the tube with respect to the coordinate system represented by the markers. These images are taken at the lowest voltages possible corresponding to about 2 kV in order to reduce the tubes to exposure.

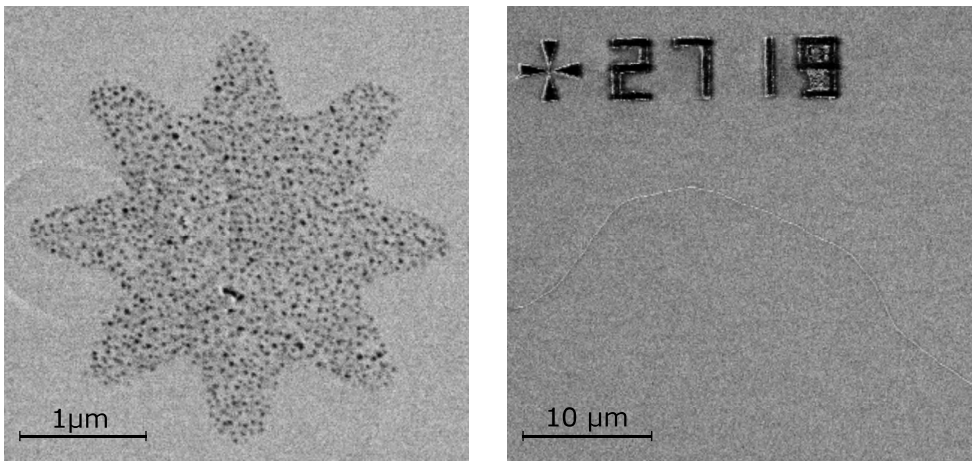

(a) Catalyst dot **(b) Carbon nanotube and marker**

Figure A.1: SEM images after carbon nanotube growth In Fig. (a), a star shaped catalyst dot is shown. Figure (b) shows a long carbon nanotube and a marker.

A.2 After stamping: adding topgate and contact lines

The sample must be bonded to the sample holder of the cryostat by means of an ultrasonic bonder and aluminium wires. However, before bonding, Cr/Au contact pads to the graphite contact lines must be fabricated. Moreover, also the Cr/Au source and drain contacts as well as the topgate contact will be added in this final EBL step.

In the last step, the sample is glued (with silver paste) on the sample holder. This silver paste is connected to one of the contact pads of the sample holder, such that it can be used as a contact to the backgate.

The sample is now ready to be bonded and to be mounted inside the measuring set-up.

Bibliography

[1] F. Duncan and M. Haldane, *Nobel Lecture : Topological quantum matter*, Review of Modern Physics **89**, 040502 (2017).

[2] A. Akhmerov, J. Sau, B. van Heck, S. Rubbert, and R. Skolansinski, *TOPOCMx: Topology in Condensed Matter*, Webcourse (date accessed: 2018-07-05), Delft University of Technology, Delft, 2014.

[3] C. W. J. Beenakker, *Search for Majorana fermions in superconductors*, Annual Review Condensed Matter Physics **4**, 113 (2013).

[4] E. Majorana, *Teoria simmetrica dell'elettrone e del positrone*, Soryishuron Kenkyu **14**, 201 (1981).

[5] A. Y. Kitaev, *Unpaired Majorana fermions in quantum wires*, Physics-Uspekhi **44**, 131 (2001).

[6] V. Mourik, K. Zuo, S. M. Frolov, S. R. Plissard, E. P. A. M. Bakkers, and L. P. Kouwenhoven, *Signatures of majorana fermions in hybrid superconductor-semiconductor nanowire devices*, Science **336**, 1003 (2012).

[7] A. Das, Y. Ronen, Y. Most, Y. Oreg, M. Heiblum, and H. Shtrikman, *Zero-bias peaks and splitting in an Al-InAs nanowire topological superconductor as a signature of Majorana fermions*, Nature Physics **8**, 887 (2012).

[8] M. Marganska, L. Milz, W. Izumida, C. Strunk, and M. Grifoni, *Majorana quasiparticles in semiconducting carbon nanotubes*, Physical Review B **97**, 7 (2018).

[9] S. Manzeli, D. Ovchinnikov, D. Pasquier, O. V. Yazyev, and A. Kis, *2D transition metal dichalcogenides*, Nature Materials **2**, 15 (2017).

[10] M. Gaaß, *The Kondo effect in single wall carbon nanotubes with ferromagnetic contacts*, PhD thesis, Universität Regensburg, 2011.

[11] K. J. G. Götz, *Carbon Nanotube quantum dots : Transport , mechanical charge detection , and fabrication development*, Phd thesis, Universität Regensburg, 2017.

[12] A. H. Castro Neto, F. Guinea, N. M. R. Peres, K. S. Novoselov, and A. K. Geim, *The electronic properties of graphene*, Review of Modern Physics **81**, 109 (2009).

[13] V. V. Schmidt, *The Physics of Superconductors*, Springer-Verlag, Berlin Heidelberg, 1997.

[14] M. Tinkham, *Introduction to superconductivity*, McGraw-Hill, Inc., New York, second edition, 1996.

[15] M. Kjaergaard, *Proximity Induced Superconducting Properties in One and Two Dimensional Semiconductors*, PhD thesis, Copenhagen University, 2015.

[16] B. T. Zhou, N. F. Yuan, H. L. Jiang, and K. T. Law, *Ising superconductivity and Majorana fermions in transition-metal dichalcogenides*, Physical Review B **93**, 180501 (2016).

[17] M. Sobhy El Sayed Bana, *Superconductivity in Two Dimensional Crystal*, Phd thesis, University of Bath, 2013.

[18] H. Wang, *Low Temperature Scanning Tunneling Microscopy and Spectroscopy : A Study On Charge Density Waves and Vortex Dynamics*, PhD thesis, University of Maryland, 2009.

[19] X. Xi, Z. Wang, W. Zhao, J. H. Park, K. T. Law, H. Berger, L. Forró, J. Shan, and K. F. Mak, *Ising pairing in superconducting NbSe2 atomic layers*, Nature Physics **12**, 139 (2016).

[20] Y. Xing, K. Zhao, P. Shan, F. Zheng, Y. Zhang, H. Fu, Y. Liu, M. Tian, C. Xi, H. Liu, J. Feng, X. Lin, S. Ji, X. Chen, Q. K. Xue, and J. Wang, *Ising Superconductivity and Quantum Phase Transition in Macro-Size Monolayer NbSe2*, Nano Letters **17**, 6802 (2017).

[21] X. Xi, H. Berger, L. Forró, J. Shan, and K. F. Mak, *Gate Tuning of Electronic Phase Transitions in Two-Dimensional NbSe2*, Physical Review Letters **117**, 106801 (2016).

[22] X. Xi, H. Berger, L. Forró, J. Shan, and K. F. Mak, *Supplementary Information: Gate tuning of electronic phase transitions in two-dimensional NbSe2*, Physical Review Letters **117**, 106801 (2016).

[23] Y. Hattori, T. Taniguchi, K. Watanabe, and K. Nagashio, *Layer-by-layer dielectric breakdown of hexagonal boron nitride*, ACS Nano **9**, 916 (2015).

[24] G. Shi, Y. Hanlumyuang, Z. Liu, Y. Gong, W. Gao, B. Li, J. Kono, J. Lou, R. Vajtai, P. Sharma, and P. M. Ajayan, *Boron nitride-graphene nanocapacitor and the origins of anomalous size-dependent increase of capacitance*, Nano Letters **14**, 1739 (2014).

[25] A. W. Tsen, B. Hunt, Y. D. Kim, Z. J. Yuan, S. Jia, R. J. Cava, J. Hone, P. Kim, C. R. Dean, and A. N. Pasupathy, *Nature of the quantum metal in a two-dimensional crystalline superconductor*, Nature Physics **12**, 208 (2016).

[26] A.-T. N-guyen, *Microfabrication of superconducting 2D NbSe2 devices in inert atmosphere*, Master thesis, Universität Regensburg, 2018.

[27] A. Seitz, *Layer-number mapping of thin NbSe2 crystals by Raman spectroscopy*, Bachelor thesis, Universität Regensburg, 2018.

[28] A. Baumgartner, G. Abulizi, K. Watanabe, T. Taniguchi, J. Gramich, and C. Schönenberger, *Carbon nanotube quantum dots on hexagonal boron nitride*, Applied Physics Letters **105**, 023111 (2014).

[29] L. Bauriedl and C. Bäuml, *Fabrication of NbSe2 to CNT contacts*, Bachelor thesis, Universität Regensburg, 2018.